Università Politecnica delle Marche
Corso di Dottorato in Scienze della Vita e dell' Ambiente
Protezione civile e ambientale

Analysis and Development of Oceanographic Models: reaching the Swash Zone

Ph.D. Dissertation of:
Francesco Memmola

Advisor:
Prof. Aniello Russo

Coadvisor:
Prof. Maurizio Brocchini

XV edition - new series

Università Politecnica delle Marche
Corso di Dottorato in Scienze della Vita e dell' Ambiente
Protezione civile e ambientale

Analysis and Development of Oceanographic Models: reaching the Swash Zone

Ph.D. Dissertation of:
Francesco Memmola

Advisor:
Prof. Aniello Russo

Coadvisor:
Prof. Maurizio Brocchini

XV edition - new series

Università Politecnica delle Marche
Corso di Dottorato in Scienze della Vita e dell' Ambiente
Dipartimento di Scienze della Vita e dell'ambiente
Via Brecce Bianche – 60131 Ancona (AN), Italy

Abstract

The swash zone is the part of the beach where the final dissipation of short-wave energy usually occurs, while low-frequency wave energy is, generally, reflected back to sea. In addition, there is generation and reflection of further low-frequency waves.

Swash zone flows are of fundamental importance not only because of their local effects but also because they can affect the surf zone dynamics as a whole. Notwithstanding its importance, typical circulation models do not account for the swash zone dynamics and simplified boundary conditions are often used, like that of perfect absorption or perfect reflection (rigid wall), at the inshore boundary of the computational domain. However, within such infinitesimal swash zone no generation or modification of low frequency waves can occur and all incoming low frequency waves are reflected at a single point.

With this contribution we explore the possibility of implementing into wave-averaged solvers, a theoretical model that gives full account, through an integral approach, of the swash zone dynamics. Once such model is implemented, the wave-averaged solver will be able to calculate the position of a mean shore line and provide along it shoreline boundary condition (SBCs) which take in account of the swash zone dynamics.

The hydrodynamic model ROMS the wave driver SWAN are either run alone into the COAWST modeling system (reference solution $\mathrm{ROMS_{rs}}$) or run in conjunction with a purpose-built routine for the calculation of the mentioned SBCs (solution $\mathrm{ROMS_{SBCs}}$ to be tested). The only forcing was provided by imposing shore-normal waves at the off-shore boundary (north edge) of the SWAN domain.

Several off-shore wave heights (H_0) and off-shore wave periods (T_0) have been used.

Use of the proposed SBCs allowed us to reproduce a shoreline close to the reference one obtained by the nearshore circulation model ROMS with about 170 nodes per wavelength cross-shore resolution, but using a much coarser grid size, up to 40 times larger. Only at resolutions about 80 times coarser than the benchmark resolution the proposed SBCs cannot properly represent the shoreline boundary.

The time needed for the simulation run with the best resolved ROMS solution is in the order of some hours, while the one carried out with the proposed SBCs and a fourty times coarser cross-shore resolution is in the order of some minutes. Hence, the great advantage, in terms of computational costs, of using the proposed SBCs is very evident.

A parametric analysis of the evolution equation for the mean shoreline reveals that the swash zone volume, seems to change in importance across different numerical experiments thus, further investigations are needed to clarify its importance. Sensitivity analyses have been carried out also to test the best location where to start the integration of the Riemann function. These analysis confirmed the importance of a good estimation of positive Riemann variable for a good estimation of the shoreline motion.

Contents

1 Introduction **1**

1.1 The nearshore zone 2

1.2 Short wave outside the surf zone 3

1.3 The Surf zone 5

1.3.1 Short wave breaking 5

1.3.2 Short waves within the surf zone 8

1.3.3 Surf zone saturation 9

1.3.4 Long waves 11

1.4 The swash zone 12

1.4.1 Swash zone hydrodynamics 13

1.5 Nearshore circulation models 15

1.5.1 Quasi-3D circulation models 17

1.5.2 Fully 3D circulation models 18

1.5.3 SHORECIRC Vs ROMS 18

1.5.4 The shoreline of wave-averaged models . . . 20

2 Methods **23**

2.1 The integral SBCs model 23

2.2 The Modeling System 30

2.2.1 The ocean model 31

2.2.2 The Wave model 34

2.2.3 The coupler 35

2.3 SBCs implementation 35

3 Results **45**

3.1 Applications 45

3.1.1 General setup 45

3.1.2 Test case 1 47

3.1.3 Test case 2 49
3.1.4 Test case 3 56
3.2 Parametric analyses 65
3.3 Fourier analysis 67

4 Discussion **75**
4.1 Integral model validation 75
4.2 Integral model parametrization 78
4.3 Wrap up section 80

List of symbols **83**
References 85

List of Figures

1.1 The Longuet-Higgins and Stewart theory of infragravity-wave formation. Wave group (blue line) and induced infragravity wave (black line). 2

1.2 Zone division of the nearshore region (from Coastal Wiki). 3

1.3 The three main types of breaking waves. All intermediate states may appear on a real beach. 6

1.4 Spilling Breakers. 7

1.5 Plunging breakers 7

1.6 Surface profile of linear wave (top panel), second-order Stokes correction profile (middle panel) and surface profile of a second-order Stokes wave (bottom panel; from Holthuijsen (2010)). 10

1.7 Surface profile of a cnoidal wave train (from Holthuijsen (2010)). 10

1.8 Illustration of the role of the SZ in generating/reflecting LFW. Wave groups reflected at a wall (panels a and c). Wave groups generating a SZ (panels b and d). Characteristic curves and shoreline position in the (x, t)-plane (panels a and b). Normalized incident (thin line) and reflected (thick line) Riemann variables at the offshore boundary (panels c and d). From Bellotti and Brocchini (2005). 20

2.1 The COAWST Modeling System that joins an Ocean model, an Atmosphere model, a Waves model, and a Sediment Transport Model for studies of coastal change 31

2.2 Representation of a typical ROMS grid (from Wiki ROMS). 32

2.3 The split time stepping used in the model (Hedström 2016). 33

2.4 Flowchart of the embedded SBCs routine. 38

2.5 Illustration of the flow representation in the (space, time) -plane near to the shoreline. The incoming characteristic curve (C_+) carries information on the incident Riemann variable(R_+) to the mean shoreline (x_l), here taken as the envelope of the run-down positions. 39

2.6 Illustration of the flow representation in the (space, time) -plane near to the shoreline. The incoming characteristic curve (C_+) carries information on the incident Riemann variable(R_+) to the mean shoreline (x_l), here taken as the envelope of the run-down positions. 40

2.7 Wedge model used as simple approximation of the swash zone region. $A =$ depth at x_l, $B = \overline{x_s - x_l}$ . . 41

2.8 Sketch of few cross-shore sections of Arakawa-C grid with x_l (pentagon) falling in different wet-dry areas. Circles represent *rho*-points while squares represent u-points, with dotted lines indicating dry nodes and solid lines indicating wet nodes: (a) x_l completely surrounded by wet points, (b) *rho*-points and u-point seaward of x_l are wet while u-point landward of x_l is dry, (c) u-points and *rho*-point seaward of x_l are wet while the *rho*-point landward of x_l is dry, (d) *rho*- and u-points seaward of x_l are wet while both *rho*- and u-points landward of x_l are dry, (e) x_l completely surrounded by dry points. 44

3.1 Bathymetry used for all the test cases. 46

3.2 Dimensionless results for Test case 1: evolution of H_0 at the offshore boundary (top-left panel); mid domain cross-shore section at different times of: wave setup (top-right panel), H (bottom-left panel) and *ubar* (bottom-right panel). 48

3.3 Shoreline (dimensionless) evolution for the first 10 minutes of runs with a $L_0/170$ cross-shore resolution. The black line represents x_l computed with $\mathrm{ROMS_{rs}}$, while the red line gives x_l computed with $\mathrm{ROMS_{SBCs}}$. 49

3.4 Evolution at x_l of the right-hand side terms of equation (2.21a), in dimensionless form: first term (black line), second term (red line), and third term (green line). 50

3.5 Shoreline (dimensionless) evolution for the first 10 minutes of run (about 120 input periods) with a $L_0/170$ cross-shore resolution (green line) and characteristic curves (equation 2.24; black lines). 50

3.6 Dimensionless results for Test case 2: evolution of H_0 at the offshore boundary (top-left panel); cross-shore section at different times of: wave setup (top-right panel), H (bottom-left panel) and *ubar* (bottom-right panel). 52

3.7 Dimensionless results for test case 2: shoreline evolution for the first 10 minutes of run (about 5 T_{tr}) using grids with different cross-shore resolution. The black lines represents x_l computed with $\mathrm{ROMS_{sl}}$, while the red lines give x_l computed with $\mathrm{ROMS_{SBCs}}$. 53

3.8 Dimensionless results for test case 2: shoreline evolution for the last 10 minutes of run (about 5 T_{tr}) using grids with different cross-shore resolution. The black lines represent x_l computed with $\mathrm{ROMS_{sl}}$, while the red lines give x_l computed with $\mathrm{ROMS_{SBCs}}$. 54

3.9 Dimensionless results for test case 2: shoreline evolution for the last 10 minutes of run (about 5 T_{tr}) using grids with different cross-shore resolution. The black lines represent x_l computed with $\mathrm{ROMS_{rs}}$, while the red lines give x_l computed with $\mathrm{ROMS_{SBCs}}$. 55

3.10 Dimensionless results for Test case 3: evolution of H_0 at the offshore boundary (top-left panel); cross-shore section at different times of: wave setup (top-right panel), H (bottom-left panel) and *ubar* (bottom-right panel). 56

3.11 Dimensionless results for Test case 3: shoreline evolution for the first 10 minutes of run (about 5 T_{tr}) using grids with different cross-shore resolution. The black lines represents x_l computed with $\mathrm{ROMS_{sl}}$, while the red lines give x_l computed with $\mathrm{ROMS_{SBCs}}$. . . 58

3.12 Dimensionless results for Test case 3: shoreline evolution for the last 10 minutes of run (about 5 T_{tr}) using grids with different cross-shore resolution. The black lines represent x_l computed with $\mathrm{ROMS_{sl}}$, while the red lines give x_l computed with $\mathrm{ROMS_{SBCs}}$. . . 59
3.13 Dimensionless results for Test case 3: shoreline evolution for the last 10 minutes of run (about 5 T_{tr}) using grids with different cross-shore resolution. The black lines represent x_l computed with $\mathrm{ROMS_{rs}}$, while the red lines give x_l computed with $\mathrm{ROMS_{SBCs}}$. . . 60
3.14 Dimensionless results for Test case 3: shoreline evolution for the last 10 minutes of run (about 5 T_{tr}; green line) and characteristic curves below it (equation 2.24; black lines). 61
3.15 Dimensionless results for Test case 3: evolution at x_l of the right-hand side terms of equation (2.21a): first term (black line), second term (green line), and third term (red line). 62
3.16 Results for Test case 3: near shoreline depth. Solution obtained with (from the top to the bottom): $\mathrm{ROMS_{rs}}$, $\mathrm{ROMS_{SBCs}}$ with $L_0/12$, $\mathrm{ROMS_{SBCs}}$ with $L_0/3$ and $\mathrm{ROMS_{SBCs}}$ with $L_0/2$. 63
3.17 Results for Test case 3: near shoreline cross-shore velocity. Solution obtained with (from the top to the bottom): $\mathrm{ROMS_{rs}}$, $\mathrm{ROMS_{SBCs}}$ with $L_0/12$, $\mathrm{ROMS_{SBCs}}$ with $L_0/3$ and $\mathrm{ROMS_{SBCs}}$ with $L_0/2$. 64
3.18 Sensitivity analysis for the function Cv. The black line represents x_l dimensionless computed with $\mathrm{ROMS_{rs}}$, while the other lines represent the dimensionless shorelines obtained with $\mathrm{ROMS_{SBCs}}$ using different values for Cv. Red line: $Cv = 0.615 - 0.201f$, blue line: $Cv = 0.400 - 0.201f$, green line: $Cv = 0.800 - 201f$, cyan line: $Cv = 0.615 - 0.101f$, grey line: $Cv = 0.615 - 0.301f$. 65

3.19 Dimensionless shoreline evolution for the last 10 minutes of run (about 5 T_{tr}). The black line is x_l obtained with $\mathrm{ROMS_{rs}}$, the red line is x_l obtained with $\mathrm{ROMS_{SBCs}}$ and the green line is x_l obtained with $\mathrm{ROMS_{SBCs}}$ excluding the third term of equation (2.21a). 66

3.20 Dimensionless results of the sensitivity analysis on the starting point for the propagation of R_+. Shoreline evolution for the last 10 minutes of run (about 5 T_{tr}) using different starting points for the propagation of R_+. The black lines represent x_l computed with$\mathrm{ROMS_{rl}}$, while the red lines give x_l computed with$\mathrm{ROMS_{SBCs}}$. 68

3.21 Dimensionless results of the sensitivity analysis on the starting point for the propagation of R_+. Shoreline evolution for the last 10 minutes of run (about 5 T_{tr}; green line) and incoming characteristic curves (equation 2.24; black lines). 69

3.22 Dimensionless results of the sensitivity analysis on the starting point for the propagation of R_+. Evolution at x_l of the right-hand side terms of equation (2.21a): first term (black line), second term (green line), and third term (red line). 70

3.23 Fourier analysis results. x_l from $\mathrm{ROMS_{rs}}$ (top panel) and its Fourier transform (bottom panel). 71

3.24 Fourier analysis results. x_l from $\mathrm{ROMS_{SBCs}}$ with a cross-shore resolution of $L_0/120$ (top panel) and its Fourier transform (bottom panel). 71

3.25 Fourier analysis results. x_l from $\mathrm{ROMS_{SBCs}}$ with a cross-shore resolution of $L_0/12$ (top panel) and its Fourier transform (bottom panel). 72

3.26 Fourier analysis results. x_l from $\mathrm{ROMS_{SBCs}}$ with a cross-shore resolution of $L_0/3$ (top panel) and its fourier transform (bottom panel). 72

3.27 Fourier analysis results. x_l from $\mathrm{ROMS}_{\mathrm{SBCs}}$ with a cross-shore resolution of $L_0/2$ (top panel) and its Fourier transform (bottom panel). 73
3.28 Fourier analysis results. The three terms of the right hand side of equation (2.21a) from $\mathrm{ROMS}_{\mathrm{SBCs}}$ with a cross-shore resolution of $L_0/2$. First term (top panel), second term (middle panel) and third term (bottom panel). 73

4.1 Mid domain cross-shore section at different times of the phase speed c (resolution of about $L_0/120$; wave height from equation (3.1)). 79

List of Tables

2.1 Definition of the introduced flow properties 24

3.1 Model parameters for the three test cases 47

Chapter 1

Introduction

The interest of scientists, coastal engineers and stakeholders in coastal environments has grown over the last 20 years with specific reference to various issues (coastal erosion, bathing water quality, runoff from rivers and dumping etc.).

The waves we normally observe when standing in front of the ocean are generated by the momentum transfer from the wind to the sea surface (Miles 1957; Phillips 1957). As waves propagate across the ocean, this energy is carried with them. When waves enter water with depth approximately half of their wavelength, they start to be affected by the sea bed. Moving shoreward waves find progressively shallow water where energy begins to dissipate through bed friction and turbulent breaking till the swash zone. Here the energy left is both dissipated or reflected back offshore. These waves are normally referred to as short waves or incident waves. This class of waves can be further subdivided into wind waves (locally generated and with frequency of few Hz and swell (generated far from the site of interest and with frequency of about $0.1Hz$)

Another very important forcing for the nearshore flows are low-frequency waves. The existence of long-period ocean waves (also called infragravity waves) has been acknowledged for some time (Munk 1949 and Tucker 1950). The amplitude of these waves was shown to have a quasi-linear relationship with the amplitude of the incident waves at the seaward limit of the surf-zone (Tucker 1950). Infragravity waves are difficult to measure and scientists

are still partly relying on theoretical approaches to describe them. One of these theories comes from the work of Longuet-Higgins and Stewart (1964), in terms of radiation stress. Since large waves have a greater radiation stress than small waves, then this difference in momentum flux causes water to be expelled from regions of larger waves to regions of smaller waves, within the group. This causes a "set down wave" which is 180° out of phase with the envelope of the wave-group, but has the same wavelength and period (see figure 1.1 for an illustration of this concept).

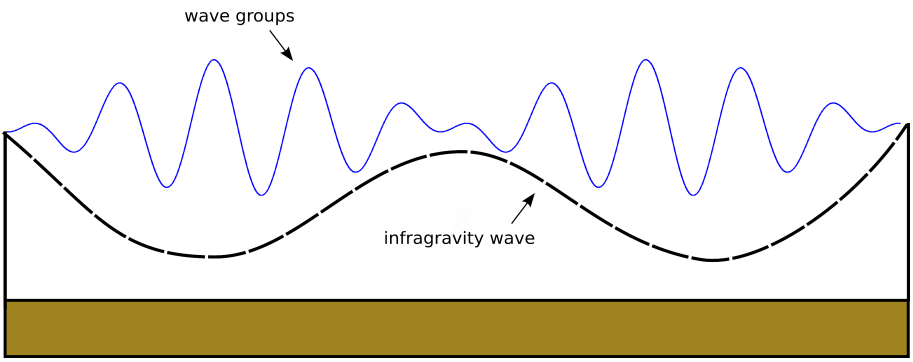

Figure 1.1: The Longuet-Higgins and Stewart theory of infragravity-wave formation. Wave group (blue line) and induced infragravity wave (black line).

An alternative theory to explain the formation of low frequency oscillations in the surf-zone was proposed by Symonds, Huntley, and Bowen (1982). Here the generation of long waves oscillation is explained as time-varying wave set-up. This because of a cross-shore variation in the position of the breakpoint due to the variation in the hight of the incident waves.

1.1 The nearshore zone

The nearshore coastal region can be defined as the region between a fictive offshore limit, which usually is considered as the limit where the depth starts to influence the waves and the shoreline. The wave

motion itself determines this depth and in simple terms it can be identified as a depth of approximately half the wave lengh. With this definition in storms with larger and longer waves the offshore limit moves further out to sea.

The nearshore zone can be schematically divided into a number of regions: the wave shoaling zone, the outer surf zone, the inner surf zone and the swash zone (see figure 1.2). The wave shoaling zone is the most offshore region. Here unbroken waves start to interact with the sea bed. In the outer surf zone waves begin to break and rapid transformation in wave shape occurs. The inner surf zone is typically characterised by the majority of waves being broken and rather slow changes in wave shape. Landward of the inner surf zone and linking the wet and dry parts of the beach, is the swash zone where waves run up and back across the beachface.

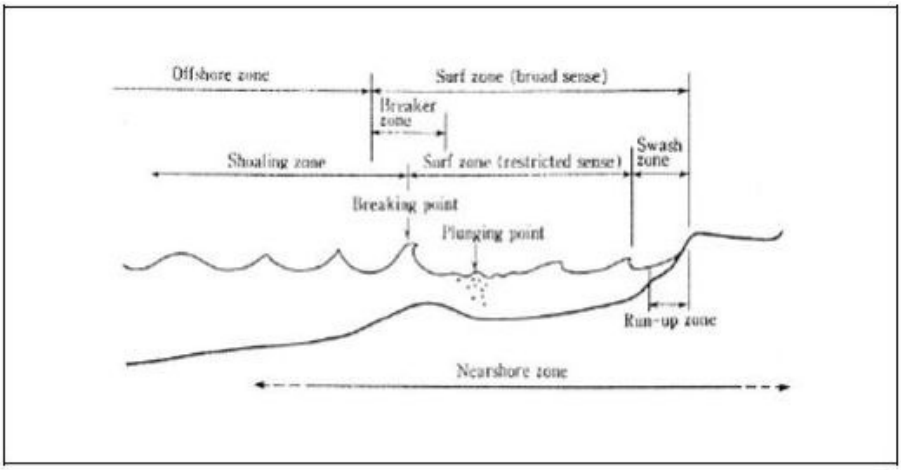

Figure 1.2: Zone division of the nearshore region (from Coastal Wiki).

1.2 Short wave outside the surf zone

In deep water the short wave profile is approximately sinusoidal in both space and time (sea figure 1.6) and is well described by the linear wave theory (Airy 1841). In the linear wave theory, the water

surface (η) is given by:

$$\eta\ (x,t) = a\cos(kx - \omega t) \tag{1.1}$$

where x is the coordinate pointing in the direction of wave propagation, t is the time, $k = \frac{2\pi}{L}$ is the wavenumber, $\omega\ = \frac{2\pi}{T}$ is the angular frequency, T is the wave period, a is the wave amplitude and L is the wavelength. The wavelength is then given by:

$$L = \frac{gT^2}{\pi}\tanh\left(\frac{2\pi d}{L}\right) \tag{1.2}$$

where g is the acceleration due to gravity and d is the water depth. The wave speed c can be calculated using:

$$c = \frac{L}{T} \tag{1.3}$$

As waves move shoreward into progressively shallower water, the wave speed decreases because the wavelength decreases. The decreases in wave length causes an increase in wave energy density due to an increase in wave height. Furthermore, the nearly sinusoidal profile that waves have is lost and waves becomes increasingly non-linear, with narrow peaked crests and wide flat troughs. The transition from linearity to non-linearity through shoaling can be represented by the Ursell parameter (Ursell 1953):

$$U_r = \frac{HL^2}{d^3} \tag{1.4}$$

with H representing the wave height. It is important to acknowledge that despite wave shoaling is most pronounced outside the surf zone, it also occurs inside the surf zone.

1.3 The Surf zone

1.3.1 Short wave breaking

A stable waveform is not possible when waves are in too shallow water, thus they break. Breaking occurs because waves become too steep, with too much energy concentrated in their front and water particles in the wave crest traveling with velocities higher than C. A "saturation type" breaking criterion gives:

$$H_{br} = \gamma_{br} d_{br} \tag{1.5}$$

where the subscript br indicates breaking conditions and γ_{br} is the breaker index, which relates the height of the breaking wave with the local water depth.

This breaking criterion and the value of γ_{br} was the subject of several studies. Battjes and Janssen (1978) re-analysed data of a number of laboratory and field experiments for various types of bottom topography and found values of γ_{br} ranging between 0.6 and 0.83. Later Kaminsky and Kraus (1993) found, using data obtained in a large number of experiments, values in the range 0.6-1.59. Clearly, γ_{br} cannot be thought of being an universal constant and its value seems to depend on both bottom slope and incident wave steepness. For instance, Battjes and Janssen (1978) suggest:

$$\gamma_{br} = \frac{H_{br}}{d_{br}} = 0.5 + 0.4 \tanh(33 s_o) \tag{1.6}$$

$s_0 = \frac{H_0}{L_0}$ being the offshore wave steepness, with H_0 the offshore wave height and L_0 the offshore wavelength. It is important to remark, that most saturation breaking conditions and indices come from laboratory experiments where purely monochromatic waves have been used.

Breaking can be classed into three types of conditions: spilling, plunging and surging breakers (see figure 1.3). Spilling breakers (figure 1.4) are associated with gently sloping beaches and steep

incident waves. They are characterised by gentle spilling of foam from the crest.

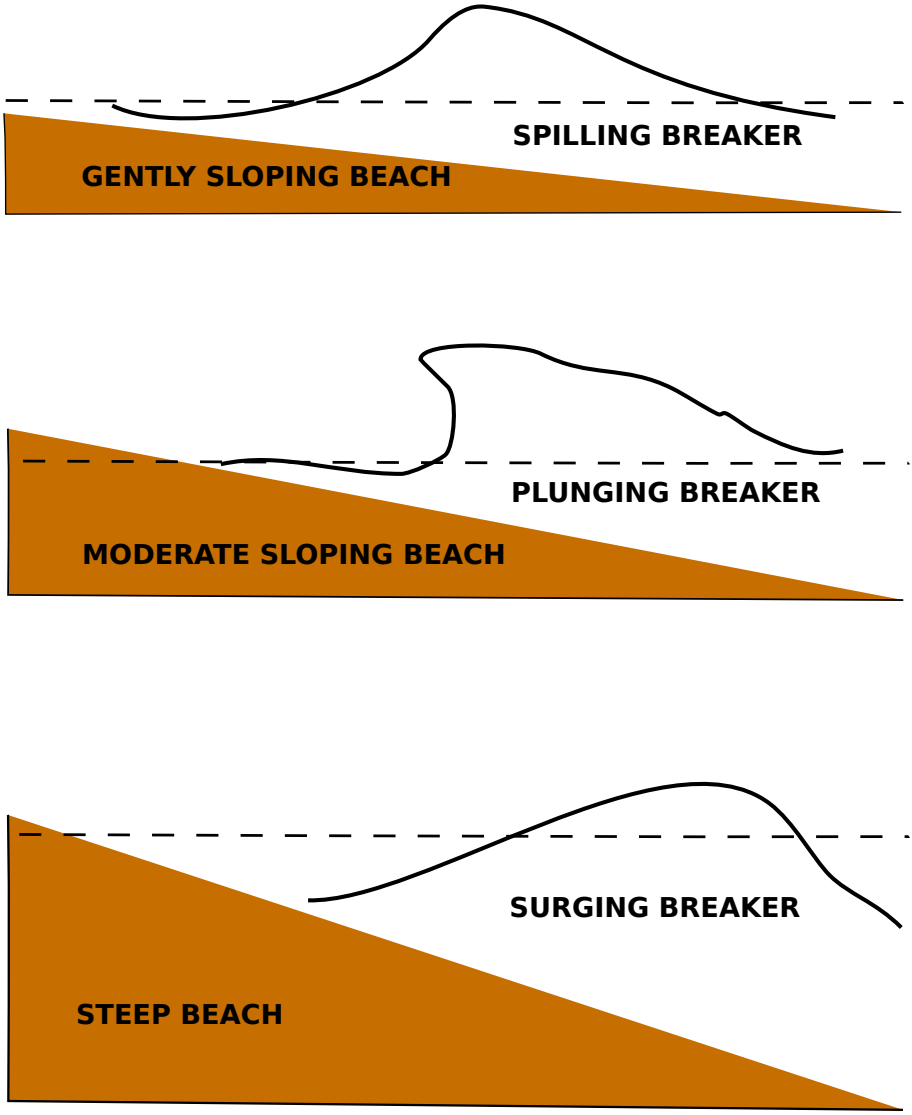

Figure 1.3: The three main types of breaking waves. All intermediate states may appear on a real beach.

Plunging breakers (figure 1.5) are associated with intermediate beach slopes and waves of intermediate steepness. In this case, the wave face becomes vertical and the crest of the wave curls over

and plunges forward and downwards. Both spilling and plunging breakers are observed in the surf zone.

Figure 1.4: Spilling Breakers.

Figure 1.5: Plunging breakers

Surging breakers occur on steep beaches with incident waves of low steepness. In surging breaker, the waves move up the beach without breaking, resulting in a large proportion of energy reflected offshore. Surging breakers are generally restricted to the swash zone.

A fourth breaking wave type was also identified by Galvin (1968): a collapsing breaker. This breaker type is intermediate between the plunging and surging breaker types.

1.3.2 Short waves within the surf zone

Energy inside the surf zone can be saturated or unsaturated. In a saturated surf zones, the wave height is dependent on local (depth) parameters and independent by the offshore wave height (Goda 1975, Wright and Short 1984, Raubenheimer and Guza 1996).

Wave characteristics keep changing as waves move through the surf zone. The current conceptual model of the surf zone divides the surf zone into outer and an inner region (Svendsen, Madsen, and Hansen 1978). The outer surf zone is where the largest waves break and where there are rapid transitions in wave shape. In the inner surf zone, most of the waves are broken and the rate of change in the wave shape is relatively slow, the waves having a quasi-steady (saw-tooth type) form throughout this region. Waves in this region are very similar to a moving bore. This region extends to the swash zone. These different regions can be parameterised in terms of the Ursell number U_r, which assumes higher values moving toward the shoreline.

The most common way to describe waves is by their (H) and (T). However, once waves enter the surf zone, they become increasingly non-linear and this parameter does not capture this change (sea figure 1.6 bottom panel). One useful parameter to capture these shape changes was described by Cowell (1982). This parameter is calculated using $\ln(e/b$, where e is the time from the minima of the preceding trough to the crest of the wave and b is the time from the crest of the wave to the subsequent trough minima.

When waves are too steep or water is too shallow, the linear wave theory is no longer valid and the waves are described through a nonlinear theory. In classical non-linear theories, flow properties are expressed as the sum of functions, dependent on the power of a perturbative parameter. Here we briefly introduce two of the classical nonlinear theories: the theory of Stokes (1847) for steep waves and the cnoidal theory for waves in shallow water (Korteweg and De Vries 1895). In the Stokes theory the basic harmonic is

corrected (second-order correction) with an 'extra' harmonic wave, written with the perturbative parameter $\epsilon = ak$ raised to the second power:

$$\eta(x,t) = \epsilon\eta_1(x,t) + \epsilon^2\eta_2(x,t) \tag{1.7}$$

where the first term on the right-hand side is the Airy wave of the linear wave theory (figure 1.6 top panel) and the second term is the second-order Stokes correction (figure 1.6 middle panel). The wave represented by equation (1.7) is called a *second-order Stokes wave.*

If depth is small the Stokes theory is no longer valid. Therefore, in addiction to, or instead of, considering nonlinear corrections due to wave steepness, corrections need to be applied to account for finite-depth effects. This is done in the theory of cnoidal waves in a fashion similar to that of Stokes theory. Here the perturbative parameter β is equal to a/d. Stopping at the second-order the surface elevation is, then, written as

$$\eta(x,t) = \beta\eta_1(x,t) + \beta^2\eta_2(x,t) \tag{1.8}$$

where, the basic wave η_1 and the extra wave η_2 are not harmonic waves but cnoidal waves (see figure 1.7).

1.3.3 Surf zone saturation

A large range of scales and types of fluid motion may be present in the inner surf zone, which will subsequently govern the shoreline oscillation and swash hydrodynamics. These include short (high-frequency) waves, long waves, edge waves, shear waves, cross-shore and longshore currents, turbulence and vortices.

Energy inside the surf zone can be saturated or unsaturated. In a saturated surf zone, the wave height is dependent on local (depth) parameters and independent of offshore wave height (sea equations 1.5 and 1.6). In contrast, unsaturated surf is defined by conditions where an increase in offshore wave height leads to an increase in surf zone wave height (Goda 1975, Wright and Short

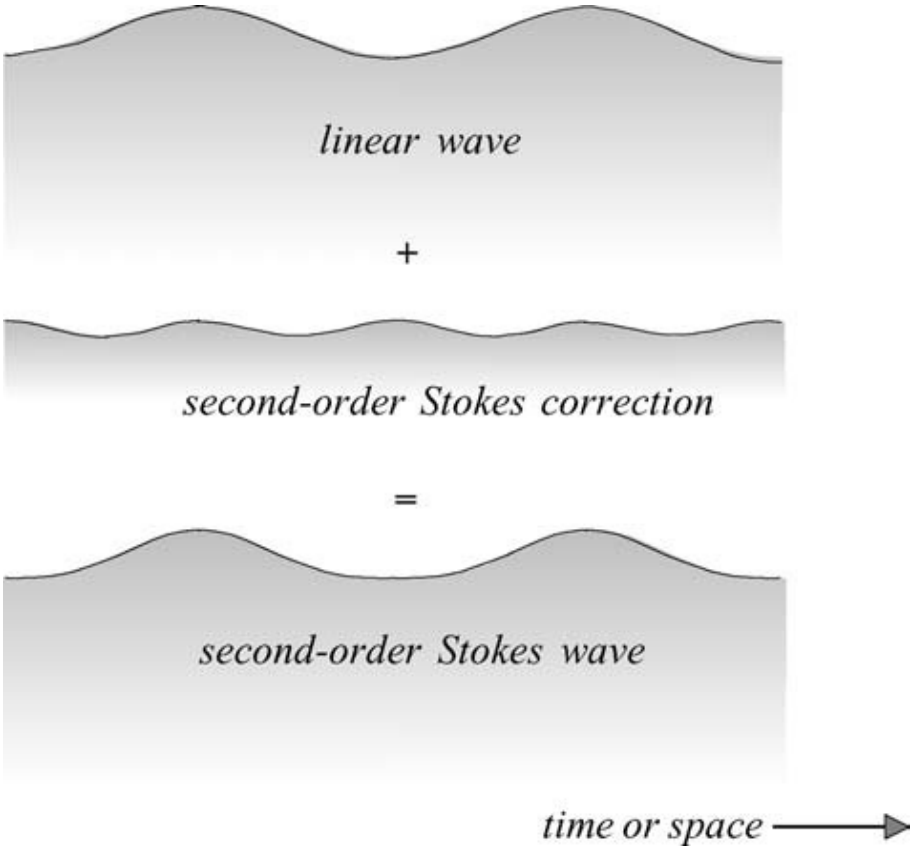

Figure 1.6: Surface profile of linear wave (top panel), second-order Stokes correction profile (middle panel) and surface profile of a second-order Stokes wave (bottom panel; from Holthuijsen (2010)).

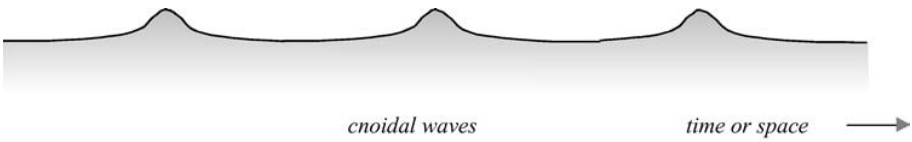

Figure 1.7: Surface profile of a cnoidal wave train (from Holthuijsen (2010)).

1984, Raubenheimer and Guza 1996). In the first case, typical of gently sloping beaches, the inner surf zone hydrodynamics may be expected to be dominated by non-breaking low-frequency waves (Huntley, Guza, and Bowen 1977, Guza and Thornton 1982, Goda 1975, Wright, Guza, and Short 1982). In unsaturated surf zones low frequency waves may still dominate the shoreline motion (Brocchini and Baldock 2008), but in addition to standing low-frequency waves a significant contribution exists from frequency down shifting (Mase 1995), wave grouping remaining in the unsaturated inner surf zone and swash-swash interactions (Baldock, Holmes, and Horn 1997).

1.3.4 Long waves

Field studies on gently sloping beaches have indicated that while the short wave energy is dissipated due to wave breaking, infragravity energy increases across the surf zone as depth decreases and it is carried through to the shoreline (Guza and Thornton 1982). Therefore, in incident-saturated conditions, the shoreline becomes increasingly long-wave dominated with increasing offshore wave height (Butt and Russell 2000)

Short waves, due to their short wavelength generally break before they reach the shoreline with subsequent energy loss. In contrast, infragravity oscillations, having a larger wavelength never become steep enough to break. However, infragravity waves do start to interact with the bottom and slow down.

The wave front slows down before the wave tail, causing an increase in amplitude with a subsequent increase in energy. Because of their low frequency, long-waves are typically reflected from the shoreline. They may either remain trapped to the shore as an edge wave (Huntley 1976), or leak out into deeper water.

Further, the interaction between the shoreward-propagating wave and its reflection from the beach face may lead to the production of a standing wave. Long waves alter the mean water depth in the surf zone on time scales ranging from 20 seconds to several

minutes. This changes the local water depth that the incident waves propagate into, this altering the propagation of the short waves.

1.4 The swash zone

The collapse of the flow on to a moving shoreline leads to flow depths at the runup tip (Shen and Meyer 1963) and throughout the swash zone that are very small when compared with the length scale of the horizontal flow. In these conditions the flow is practically tangential to the beach, which allows for use of the Nonlinear Shallow Water Equations (NSWEs) as the preferential tool to study this part of the foreshore with good confidence (Peregrine 1972, Brocchini and Baldock 2008).

Although the swash zone moves over the whole of the intertidal zone, the local swash zone may be defined as the region of the foreshore where the wave action (uprushes and backswashes) moves the instantaneous shoreline back and forth around the mean water level (Holman 1986, Elfrink and Baldock 2002). The moving shoreline makes this area to be alternatively exposed to the atmosphere or covered by water thus, flow properties here are only defined for short intervals (Brocchini and Baldock 2008).

The swash zone is arguably the most complex area of the coastline. It can be seen as a highly dynamic and changeable boundary layer between land and sea, where many hydrodynamics and morphological events occur over a wide range of time scales. Swash motions are characterized by a great turbulence level, highly unsteady flows, considerable sediment transport and rapid morphological changes (Brocchini 1997, Puleo et al. 2000, Masselink and Puleo 2006, Brocchini and Baldock 2008).

This region is well defined for monochromatic waves while this is not true for real sea states where runup and rundown and setup vary constantly with time. In this context, the swash zone may be defined as the region in which the beach face is intermittently exposed to the atmosphere, possibly over both long (minutes) and short (sec-

onds) time scales (Elfrink and Baldock 2002). Two broadly different types of swash oscillations have been identified by theoretical, field and laboratory studies, consistent with the forcing at the seaward swash boundary (see section 1.3.3). Typically swash motions may result from non-breaking standing waves or broken short waves.

1.4.1 Swash zone hydrodynamics

Swash zone boundary conditions

The swash zone hydrodynamics is mainly forced by boundary conditions imposed by the inner surf zone and beachface features. Along this boundary the forcings include wave or bore height, period, waveshape, orbital velocities, currents, turbulence, beach slope and beach composition (Elfrink and Baldock 2002). From the above it is clear that, in order to properly predict the swash zone hydrodynamics, it is crucial to have a thorough understanding of the inner surf zone processes (see 1.3.3).

Swash oscillations

The swash motion features change depending on the beach configuration, hydraulic forcing and gradient and mean sediment size. Thus, an unambiguous definition of swash characteristics is not really possible.

One classification based on beach topography divides into swash zones typical of dissipative beaches and reflective beaches. Dissipative beaches are generally typified by a gently sloping bathymetry and relatively fine sediments. In this condition the surf zone is normally saturated and the swash motion is imposed by low frequency oscillations, being the short wind wave energy dissipated through a wide surf zone. In contrast, reflective beaches feature steeper gradients where most of the wave energy is reflected offshore and the only swash is due to bores collapsing at the shoreline. Here the dominant swash motion is defined by the incoming short wave

approaching the beach face as breaking bores. In parallel with this considerations typical swash periods may range from seconds on steep, reflective beaches, to minutes on gentle, dissipative beaches (Hughes, Masselink, and Brander 1997, Butt and Russell 1999). Generally, in both cases the swash zone works as a dissipation area for high frequency waves, while long waves are reflected seaward (Brocchini and Baldock 2008)

It is obvious that the only-dissipative or the only-reflective case are just a theoretical matter. On natural beaches real swashes are always driven by both short and long waves.

The high complexity of the swash zone dynamics suggests to neglect bottom friction and flow infiltration/exfiltration across the bed boundary to give a first description of it. With this simplified approach a single runup event consequent to an incident broken wave (surf zone bore) propagating perpendicular to the coast can be described as follows:

1. At the breakpoint the wave starts to dissipate energy because of breaking-induced turbulence, with a consequent H decrease.

2. In the surf zone the wave height decreases approximately as a linear function of the water depth.

3. Approaching the local instantaneous shoreline (zero depth), the bore front and the water behind the bore front abruptly accelerate (Whitham 1958, Brocchini and Baldock 2008) and the bore collapses (swash uprush) (Shen and Meyer 1963, Brocchini and Baldock 2008) with its potential energy being suddenly transformed into the kinetic energy of a thin wedge of water whose tip propagates up the beach face.

4. Once the swash has reached its maximum uprush, the flow reverses and accelerates offshore forming the backswash. As for the uprush, the swash surface is seaward dipping for the whole of the backwash phase. It is important to note that the flow reversal does not occur simultaneously at all cross-shore locations (Hibberd and Peregrine 1979). In general, the uprush is of shorter duration compared to the backwash but has flow velocities of greater absolute

magnitude (Hughes, Masselink, and Brander 1997).

Swash-swash interaction

When a sequence of waves approaches the beach, the intensity of the swash-swash interaction within the surf zone can be described by the ratio between the period T_s of a individual swash event and the incident wave period T. If $T > T_s$ normally there is little or no interaction, while the case of $T_s \geq T$ corresponds to strong interaction.

Swash-swash interactions occur when there is interaction between incident waves and the runup or backwash of the preceding waves. These interactions generate a broad range of scales and new motions comprising: low-frequency waves, backwash bores and hydraulic jumps, and turbulence (Brocchini and Baldock 2008).

The interaction between high-frequency swash and standing long waves in the swash zone is also a very important feature for both the hydrodynamics and the beach face morphology. The long waves act likewise a tide, moving the short-wave swash across the beach face increasing the active swash zone width (Brocchini and Baldock 2008).

Short-wave runup may coincide with the standing wave runup increasing swash amplitudes through constructive interference. Destructive interference occurs if runup and backwashes oppose each other (Brocchini and Baldock 2008).

1.5 Nearshore circulation models

In the last 40 years Boussinesq-type models (BTMs) became the most used tools for coastal-type computations. The reason for this success is their ability to represent all main physical phenomena and their numerical cheapness (Brocchini 2013). Boussinesq (1872), was the first to tackle the problem of solving the Navier Stokes equations in shallow waters. With the increase of computation power, com-

puters became available for scientific-purpose calculations. Thus, it was possible to couple the power of mathematical and numerical techniques and, hence, the pioneering contribution by Peregrine (1967).

Two classes of BTMs rise, distinguishing between: BTMs with the assumption of irrotational flow and BTMs which compute rotational flow. In the former class, vorticity injection at the bottom and free-surface boundary layers are taken as negligible. For this kind of BTMs, breaking dissipation and parametrized bottom friction need to be externally added (Brocchini 2013). The external breaking-induced dissipation can be based on the 'surface roller' concept (Svendsen 1984). Different is the situation for the latter class where, dissipative mechanisms induced by wave breaking, rather than being externally added, naturally stem from the equation derivation procedure (Veeramony and Svendsen 2000). This class of BTMs seems to be more suited to reproduce surf zone flows. However, they require closures for both vorticity and turbulence (Brocchini 2013). The class of 'rotational flow' BTMs even though used for scientific studies, are practically no used at the operational level. The reasons for such a partial success are several, among the most important: the difficulty in physically describing the required closures and numerically implementing them into an efficient code (Brocchini 2013).

The temporal evolution of Boussinesq-type models has been mainly pushed by practical requirements. In particular, the coastal engineering community has been largely involved in the process of extending the region of validity of BTMs towards the intermediate-to-deep waters, on one hand, and towards the near-shoreline dynamics on the other hand.

In early BTMs, the effects of nonlinearity were treated as a weak perturbation to a primarily linear problem. However, in many practical cases (i.e. shoaling waves and breaking waves), nonlinear effects are too strong and this kind of approach is not efficient anymore and a fully nonlinear approach is necessary. This was the

focus of research in BTMs over the first decade of the 2000s (Madsen, Bingham, and Schäffer 2003, Madsen, Fuhrman, and Wang 2006, Bingham, Madsen, and Fuhrman 2009).

Computations of coastal flows is normally carried out either at a wave-resolving or at a wave-averaged level. However, when attempting very long simulations over spatial areas of the order of $10Km^2$ or larger the limits of wave-resolving models come out. When this kind of computations is needed the best solution is to resort to wave-averaged models.

Averaging shallow-water-type equations over the period of short waves leads to wave-averaged two-dimensional horizontal (2DH) models, where the closure problem is that of representing the unresolved short-wave motion. These contributions appear in the momentum equation as radiation stresses. Ever since the concept of radiation stress was presented by Longuet-Higgins and Stewart (1964) nearshore simulations have been carried out by wave-averaged models.

The first of these wave-averaged models were relatively simple theoretical solutions of longshore currents driven by radiation stress gradients (Longuet-Higgins 1970). One of the first numerical models for nearshore circulation was developed by Noda (1974). The model was used to study steady flows with longshore varying topography and to model circulation patterns with rip currents. Other important early nearshore circulation models were those by Ebersole and Dalrymple (1980) and Wu and Liu (1985). These models were all 2DH models, which, essentially solve the shallow water equations.

1.5.1 Quasi-3D circulation models

The development of quasi-3D models began with De Vriend and Stive (1987) who divided the currents into primary and secondary components. The primary current was forced by the depth-invariant terms (i.e. the pressure gradient) while the secondary current was

driven by the depth-varying forcing. Alternatively, Svendsen and Lorenz (1989) assumed the cross-shore and longshore currents were weakly dependent on each other, this resulting in a current profile with a spiral shape. Svendsen and Putrevu (1990) solved the vertical profiles and used the result in a depth-averaged numerical model. Svendsen and Putrevu (1994) found that the current-current and wave-current interaction terms were inducing non-linear mixing many times stronger than the turbulent mixing from wave breaking. A generalized version of these mixing terms was derived by Putrevu and Svendsen (1999). A simplified version of the 3D dispersive mixing is included in the nearshore circulation model SHORECIRC, as described by Svendsen, Haas, and Zhao (2002) and Haas, Svendsen, et al. (2003).

The primary advantage of quasi-3D models is that they solve for the vertical variation of the currents and included the leading-order effect of the depth-varying currents on the depth-averaged flow field all on a two-dimensional grid, preserving the computational speed of a 2DH model.

1.5.2 Fully 3D circulation models

In the last years several effort even been put to introduce the effects of waves on ocean currents using fully three dimensional numerical models. Some of the most successful works were carried out with the Regional Ocean Modeling System (ROMS) Haas, Svendsen, et al. (2003), Haidvogel et al. (2008), Shchepetkin and McWilliams (2005), and Uchiyama, McWilliams, and Shchepetkin (2010). See section 2.2.1 for a detailed description of ROMS.

1.5.3 SHORECIRC Vs ROMS

Haas and Warner (2009) compared the quasi-3D SHORECIRC circulation model to the fully 3D ROMS circulation model for test case called "Shoreface". In the following we recall the main conclusions of their work.

The two models' performances are compared for three wave conditions: 1) spectral waves approaching a plane beach with an oblique angle of incidence; 2) monochromatic waves driving longshore currents in a laboratory basin; and 3) monochromatic waves on a barred beach with rip channels in a laboratory basin.

For tests 1 and 2, depth-averaged quantities are nearly identical for the two models and similar results for the same quantities for the two models are also found for test case 3. The small differences observed in the latter test are due to either different boundary conditions or different turbulence closures used in the two models. The differences in the vertical variation of the currents between the two models are primarily a result of the method for incorporating the vertical variation of the radiation stresses.

Being ROMS a 3D model, the radiation stresses parameterization allows for vertical variability. On the other hand, in SHORECIRC, in order to simplify the integration of the depth varying currents, the long wave theory for a sloping bottom is used for the formulation of the radiation stress terms in the momentum equations that retain vertical flow variability. However, in the depth-averaged equations of SHORECIRC, the radiation stress terms are calculated with the linear theory of waves evolving over a horizontal seabed. This creates an inconsistency between the two radiation stress forcing. For both models, there is a local imbalance over the depth between the terms that are balanced in the depth-integrated momentum equations. For ROMS this is mainly due to the vertical variation of the radiation stress whereas, for SHORECIRC it is a consequence of the above mentioned over-simplified calculation of the radiations stresses. This imbalance is generally compensated by the vertical viscosity term, resulting in differing vertical variation of the currents for the two models.

The quasi-3D model is computationally faster when run on a single processor. However ROMS is designed to use either OpenMP (shared memory) or MPI (distributed memory) systems, thus, the overall computational speed of ROMS can be faster. Further, the

fully 3D model can be applied to include more processes like river flows, tracer advection, stratification, Coriolis forcing, and can span across a broader range of spatial applicability.

1.5.4 The shoreline of wave-averaged models

The use of these models allowed a good representation of the phenomena evolving in the nearshore area, especially when coupled to wave drivers to represent the effects of waves on ocean currents. Although well developed, wave-averaged models use some assumptions that limit their capability of reproducing natural flow conditions. One of the most crucial shortcomings concerns the representation of the swash zone dynamics. Typical circulation models use simplified boundary conditions such that perfect absorption or perfect reflection (rigid wall) is enforced at the inshore boundary of the computational domain.

However, within the infinitesimal swash zone prescribed through a wall condition no generation or modification of low-frequency waves can occur and all incoming low frequency waves are reflected at a single point (Brocchini and Baldock 2008).

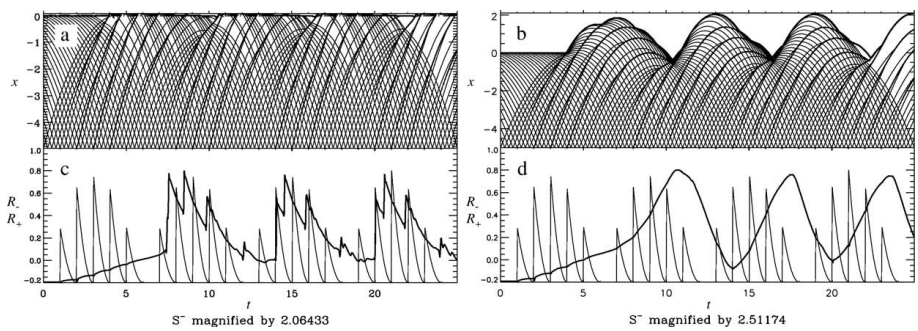

Figure 1.8: Illustration of the role of the SZ in generating/reflecting LFW. Wave groups reflected at a wall (panels a and c). Wave groups generating a SZ (panels b and d). Characteristic curves and shoreline position in the (x, t)-plane (panels a and b). Normalized incident (thin line) and reflected (thick line) Riemann variables at the offshore boundary (panels c and d). From Bellotti and Brocchini (2005).

The present thesis work explores the possibility of implementing into available wave-averaged solvers, a theoretical model (Brocchini and Peregrine 1996, Brocchini and Bellotti 2002, Antuono, Brocchini, and Grosso 2007) that gives full account, through an integral approach, of the swash zone dynamics. Once such model is implemented, the wave-averaged solver will be able to calculate the position of a mean shoreline and provide along it shoreline boundary condition (SBCs) that take in account of the swash zone dynamics (see section 2.3 for the description of the theoretical model).

Chapter 2

Methods

2.1 The integral SBCs model

A detailed description of the integral model SBCs by Brocchini & Coauthors is given in the following. Suitable boundary conditions are defined for wave-averaged models that fully take account of the swash zone dynamics. All the contents and materials used in this section come from Brocchini and Peregrine (1996) and Brocchini and Bellotti (2002). The new boundary condition are based on the NLSWE. These equation are depth integrated and obtained by assuming that vertical accelerations of water, or those normal to the beach, are negligible compared with gravity. The general set of dimensionless NLSWE (no specific notation is used for dimensionless variables) put in conservation form and completed with the energy equation and a dimensionless bed friction $\vec{\tau} = (\tau_1, \tau_2)$ is:

$$d_t + (ud)_x + (vd)_y = 0, \tag{2.1a}$$

$$(ud)_t + (u^2 d + \frac{1}{2}d^2)_x + (uvd)_y + d + \tau_1 = 0, \tag{2.1b}$$

$$(vd)_t + (uvd)_x + (v^2 d + \frac{1}{2}d^2)_y + \tau_2 = 0, \tag{2.1c}$$

$$\begin{aligned} &\frac{1}{2}[d(u^2+v^2)+d^2]_t + (\frac{1}{2}u^3 d + \frac{1}{2}v^2 ud + ud^2)_x + \\ &(\frac{1}{2}v^3 d + \frac{1}{2}u^2 vd + vd^2)_y + u(d+\tau_1) + v\tau_2 = 0, \end{aligned} \tag{2.1d}$$

Table 2.1: Definition of the introduced flow properties

Name	Explicit expression	Flow property
Q_μ	$u_\mu d$	Local mass flow
$S_{\mu\nu}$	$u_\mu u_\nu d + \delta_{\mu\nu}\frac{1}{2}d^2$	Local momentum flux tensor
F	$\frac{1}{2}\mathbf{u}^2 + d$	Local energy density
V	$\int_{x_l}^{x_h} d dx$	Volume of water in swash zone
P_μ	$\int_{x_l}^{x_h} Q_\mu dx$	Momentum of water in swash zone
$M_{\mu\nu}$	$\int_{x_l}^{x_h} S_{\mu\nu} dx$	Integrated momentum flux tensor
E	$\int_{x_l}^{x_h} (\frac{1}{2}\mathbf{u}^2 d + d^2) dx$	Energy of water in swash zone
Υ_μ	$\int_{x_l}^{x_h} \tau_\mu dx$	Friction force in swash zone
Γ	$\int_{x_l}^{x_h} u_\mu \tau_\mu dx$	Work done by friction in swash zone

where u and v are, respectively, the cross-shore component and the long-shore component of the flow velocity. The swash zone limits are x_l, the seaward (lower) and x_h shoreward (higher) limits. The seaward boundary may be chosen to be the lowest limit x_l, of the moving shoreline in a group of waves. Integration of equations (2.1) over the swash zone width for constant x_l gives:

$$\frac{\partial V}{\partial t} = \int_{x_l}^{x_h} d_t dx = Q_1(t)|_{x_l} - \frac{\partial P_2}{\partial y}, \tag{2.2a}$$

$$\frac{\partial P_1}{\partial t} = \int_{x_l}^{x_h} (ud)_t dx = S_{11}(t)|_{x_l} - V(t) - \frac{\partial M_{12}}{\partial y} - \Upsilon_1(t), \tag{2.2b}$$

$$\frac{\partial P_2}{\partial t} = \int_{x_l}^{x_h} (vd)_t dx = S_{12}(t)|_{x_l} - V(t) - \frac{\partial M_{22}}{\partial y} - \Upsilon_2(t), \tag{2.2c}$$

$$\begin{aligned} \frac{\partial E}{\partial t} &= \int_{x_l}^{x_h} [\frac{1}{2}(u^2 + v^2)d + d^2]_t dx \\ &= F(t)Q_1(t)|_{x_l} - P_1(t) - \frac{\partial}{\partial y}\int_{x_l}^{x_h} FQ_2 dx - \Gamma_t, \end{aligned} \tag{2.2d}$$

These equations introduce flow properties integrated over the swash zone which are listed in table 2.1 where $\vec{u} = (u_1, u_2)$. The integral flow properties, then, are used to seek appropriate boundary conditions at the seaward swash zone limit for wave-averaged models. This requires the knowledge of both long-wave motions and short-

wave motions contributes at the boundary x_l.

To obtain dynamic equations suitable for wave-averaged model the basic flow properties u, v and d are splitted using a Reynolds-type decomposition into long-period and short-period properties:

$$u = \langle u \rangle + \tilde{u}, \quad v = \langle v \rangle + \tilde{v}, \quad d = \langle d \rangle + \tilde{d}, \quad \langle \tilde{u} \rangle = \langle \tilde{v} \rangle = \left\langle \tilde{d} \right\rangle = 0. \tag{2.3}$$

Here $\langle u \rangle$, $\langle v \rangle$ and $\langle d \rangle$ come from all motions whose typical time scale is significantly longer than the typical short-wave period. Whereas $\tilde{u}$, $\tilde{v}$ and $\tilde{d}$ contributes are due to short-wave motions. By substituting in the shallow water equations (2.1) for each flow variable and by phase averaging, a set of equations for long-period flow properties is obtained:

$$\frac{\partial \langle d \rangle}{\partial t} + \frac{\partial}{\partial x}\left[\langle u \rangle \langle d \rangle + \left\langle \tilde{Q}_1 \right\rangle\right] + \frac{\partial}{\partial y}\left[\langle v \rangle \langle d \rangle + \left\langle \tilde{Q}_2 \right\rangle\right] = 0 \tag{2.4a}$$

$$\begin{aligned} &\frac{\partial}{\partial t}\left[\langle u \rangle \langle d \rangle + \left\langle \tilde{Q}_1 \right\rangle\right] + \frac{\partial}{\partial x}\Big[\langle d \rangle \Big(\langle u \rangle^2 + \langle \tilde{u} \rangle^2 + \\ &\frac{1}{2}\langle d \rangle\Big) + 2\langle u \rangle \left\langle \tilde{Q}_1 \right\rangle + \left\langle \tilde{S}_{11} \right\rangle\Big] + \frac{\partial}{\partial y}\Big[\langle d \rangle \Big(\langle u \rangle \langle v \rangle + \\ &\langle \tilde{u}\tilde{v} \rangle\Big) + \langle u \rangle \langle Q_2 \rangle + \langle v \rangle \langle Q_1 \rangle + \left\langle \tilde{S_{12}} \right\rangle\Big] + \langle d \rangle = 0 \end{aligned} \tag{2.4b}$$

$$\begin{aligned} &\frac{\partial}{\partial t}\left[\langle v \rangle \langle d \rangle + \left\langle \tilde{Q}_2 \right\rangle\right] + \\ &\frac{\partial}{\partial y}\left[\langle d \rangle \left(\langle v \rangle^2 + \langle \tilde{v} \rangle^2 + \frac{1}{2}\langle d \rangle\right) + 2\langle v \rangle \left\langle \tilde{Q}_2 \right\rangle + \left\langle \tilde{S}_{22} \right\rangle\right] + \\ &\frac{\partial}{\partial x}\left[\langle d \rangle \left(\langle u \rangle \langle v \rangle + \langle \tilde{u}\tilde{v} \rangle\right) + \langle v \rangle \langle Q_1 \rangle + \langle u \rangle \langle Q_2 \rangle + \left\langle \tilde{S_{12}} \right\rangle\right] = 0 \end{aligned} \tag{2.4c}$$

The same Reynolds-type decomposition is used inside the swash zone. The decomposition is achieved by assuming the swash motion is almost entirely assigned to short-wave contributions and that the

only long-wave contributions comes from parameterizing from the motion of the mean shoreline x_l and longshore drift due to wave breaking parameterized by longshore current velocity $W = W(y,t)$.

In similar fashion to equation (2.3), which applies outside the swash zone, properties are separated into short-wave and long-wave contributions inside the swash zone.

$$d = \hat{d}, \quad u = \frac{\partial x_l}{\partial t} + \hat{u}, \quad v = W + \hat{v} \tag{2.5}$$

To obtain an explicit expression of the first boundary condition we consider the flow of mass into the swash zone relative to $x = x_l$. The wave average of equation (2.2a) is:

$$\frac{\partial \langle V \rangle}{\partial t} + \frac{\partial \langle P_2 \rangle}{\partial y} = \langle Q_1 \rangle |_{x_l} \tag{2.6}$$

where now the right-hand side contains the relative flow velocity $(u - \frac{\partial x_l}{\partial t})$. The left-hand side is also rewritten in terms of the local variables inside the swash zone. Dividing the integrated longshore momentum P_2 between long and short waves we obtain:

$$\frac{\partial \left\langle \hat{V} \right\rangle}{\partial t} + \frac{\partial \left\langle W\hat{V} \right\rangle}{\partial y} + \frac{\partial \left\langle \hat{P}_2 \right\rangle}{\partial y} = \langle u \rangle \langle d \rangle + \left\langle \tilde{u}\tilde{d} \right\rangle - \frac{\partial x_l}{\partial t} \langle d \rangle \tag{2.7}$$

The first term on the left-hand side of this equation is the rate of change of the total volume of water in the swash zone; the second and third terms are the change in volume of water due to the lateral variation of longshore currents, respectively associated with the longshore velocity inside the swash zone W and with the wave contribution $\left\langle \hat{P}_2 \right\rangle$.

A similar derivation for the dimensional average balance of the onshore momentum inside the swash zone, with a beach slope α

gives:

$$\begin{aligned}
&\frac{\partial}{\partial t}\left[\left\langle \hat{P}_1 \right\rangle + \frac{\partial x_l}{\partial t}\left\langle \hat{V} \right\rangle\right] + \frac{\partial \left\langle W\hat{P}_1 \right\rangle}{\partial y} + \\
&\frac{\partial \left\langle \hat{M}_{12} \right\rangle}{\partial y} + \frac{\partial x_l}{\partial t}\left[\frac{\partial \left\langle W\hat{V} \right\rangle}{\partial y} + \frac{\partial \left\langle \hat{P}_2 \right\rangle}{\partial y}\right] + g\alpha\left\langle \hat{V} \right\rangle + \langle \Upsilon_1 \rangle = \\
&\left(\langle u \rangle - \frac{\partial x_l}{\partial t}\right)^2 \langle d \rangle + \frac{1}{2} g \langle d \rangle^2 + 2\left\langle \tilde{u}\tilde{d} \right\rangle = \\
&\left(\langle u \rangle - \frac{\partial x_l}{\partial t}\right) + \left\langle \tilde{u}^2 \right\rangle \langle d \rangle + \left\langle \tilde{u}^2 \tilde{d} \right\rangle + \frac{1}{2} g \left\langle \tilde{d}^2 \right\rangle
\end{aligned} \tag{2.8}$$

The first two terms on the left-hand side are the rate of change of the mean momentum in the swash zone. All the terms with y-derivatives are the contributions due to longshore velocity gradients, including both long-period contributions and short-period contributions. Conservation of the longshore momentum similarly yields:

$$\begin{aligned}
&\frac{\left\langle \partial W\hat{V} \right\rangle}{\partial t} + \frac{\partial \left\langle \hat{P}_2 \right\rangle}{\partial t}\frac{\partial \left\langle W^2\hat{V} \right\rangle}{\partial y} + 2\frac{\partial \left\langle W\hat{P}_2 \right\rangle}{\partial y} + \frac{\partial \left\langle \hat{M}_{22} \right\rangle}{\partial y} + \langle \Upsilon_2 \rangle \\
&= \left(\langle u \rangle - \frac{\partial x_l}{\partial t}\right)\langle v \rangle \langle d \rangle + \langle \tilde{u}\tilde{v} \rangle \langle d \rangle + \left\langle \tilde{u}\tilde{d} \right\rangle \langle v \rangle \\
&+ \left\langle \tilde{v}\tilde{d} \right\rangle \left(\langle u \rangle - \frac{\partial x_l}{\partial t}\right) + \left\langle \tilde{u}\tilde{v}\tilde{d} \right\rangle
\end{aligned} \tag{2.9}$$

The above three equations are boundary conditions for the long-wave motion. Here the mean shoreline x_l represents the envelope of the rundown positions. Use of the envelope of the rundown positions as mean shoreline, has the great advantage that flow properties may unambiguously be defined, being this the only part of the swash zone always wet.

In a later effort Brocchini and Bellotti (2002) derived simplified SBCs for one-dimensional flow from the boundary conditions of Brocchini and Peregrine (1996). In the case of 1DH flow, propa-

gation equations which hold at x_l are immediately obtained from equations (2.7) and (2.8).

$$\frac{dx_l}{dt} = \langle u \rangle + \frac{\left\langle \tilde{u}\tilde{d} \right\rangle - d\left\langle \hat{V} \right\rangle / dt}{\langle d \rangle} \tag{2.10}$$

$$\begin{aligned} &\frac{d}{dt}\left[\left\langle \hat{P}_x \right\rangle + \frac{dx_l}{dt}\left\langle \hat{V} \right\rangle\right] + g\alpha\left\langle \hat{V} \right\rangle + \langle \Upsilon_x \rangle = \left[u - \frac{dx_l}{dt}\right]^2 d + \\ &2\left\langle \tilde{u}\tilde{d} \right\rangle \left[\langle u \rangle - \frac{dx_l}{dt}\right] + \left\langle \tilde{u}^2 \right\rangle \langle d \rangle + \left\langle \tilde{u}^2\tilde{d} \right\rangle + \frac{g}{2}[\left\langle \tilde{d}^2 \right\rangle + \langle d \rangle^2] \end{aligned} \tag{2.11}$$

In order to use the SBCs, it is necessary to write them in a form consistent with the flow description employed in available wave-averaged models. In models like ROMS and SHORECIRC the mean flow velocity $\bar{u}$ is defined as the time-average of the total mass flux divided by the mean depth. Thus, in these models $\bar{u}$ is used rather than the mean velocity $\langle u \rangle$. Concerning the definition of the mean water depth there is no ambiguity between $\bar{d}$ and $\langle d \rangle$. Here $\bar{d}$ is used just to be consistent with the notation:

$$\bar{d} = \langle d \rangle \,, \quad \bar{u} = \langle u \rangle + \frac{\tilde{u}\tilde{d}}{\langle d \rangle} \tag{2.12}$$

Hence substitution of (2.12) in equations (2.10) and (2.11) gives:

$$\frac{dx_l}{dt} = \bar{u} - \frac{1}{\bar{d}}\frac{d\left\langle \hat{V} \right\rangle}{dt} \tag{2.13}$$

$$\begin{aligned} \frac{d}{\text{ṭ}}\left[\left\langle \hat{P}_x \right\rangle + \frac{dx_l}{dt}\left\langle \hat{V} \right\rangle\right] + g\alpha\left\langle \hat{V} \right\rangle + \langle \Upsilon_x \rangle = \left[\bar{u}^2 + \left(\frac{dx_l}{dt}\right)^2\right]\bar{d} \\ -2\bar{u}\bar{d}\frac{dx_l}{dt} + \left\langle \bar{u}^2 \right\rangle + \frac{g}{2}\bar{d}^2 - \frac{\left\langle \tilde{Q} \right\rangle}{d} + \left\langle \tilde{S} \right\rangle \end{aligned} \tag{2.14}$$

A third equation is required for completely solving for the mean flow, i.e. determining both the motion of x_l and the value of both $\bar{d}(x_l)$ and $\bar{u}(x_l)$. Such information is carried by the positive Riemann variable $R_+ = \bar{u} + \sqrt{g\bar{d}}$ which propagate from the interior toward the shoreline along positive characteristics of the NLSWE

for the mean flow (Özkan-Haller and Kirby 1997)

$$\frac{dR_+}{dt} = -g\alpha - \frac{1}{\bar{d}}\frac{d\left\langle \tilde{S} \right\rangle}{dx} \quad \text{along} \quad \frac{dx}{dt} = \bar{u} + \sqrt{g\bar{d}} \tag{2.15}$$

An approximation of equation (2.14) was derived on the basis of results of numerical solutions of the NLSWE. Hence, a large number of solutions was used to asses the relative size of each term of equation (2.14) giving the simplified form:

$$g\bar{d}^3 - 2\Big[g\alpha\left\langle \hat{V} \right\rangle + \langle \Upsilon_x \rangle - \left\langle \tilde{S} \right\rangle\Big]\bar{d} - 2\left\langle \tilde{Q} \right\rangle^2 = 0 \tag{2.16}$$

Dimensional arguments and analytical results based on the Carrier and Greenspan solution (e.g. Mei 1989) and the Shen and Mayer solution (e.g. Peregrine and Williams 2001) and fitting of a large number of solutions, led to the following relations between swash zone properties and H:

$$\begin{gathered} \left\langle \hat{V} \right\rangle = C_V\frac{H^2}{\alpha}, \quad \left\langle \tilde{Q} \right\rangle = C_Q\sqrt{gH^3}, \quad \left\langle \tilde{S} \right\rangle = C_S g H^2, \\ \langle \Upsilon_x \rangle = C_\Upsilon g H^2, \quad \frac{d\left\langle \hat{V} \right\rangle}{dt} = \frac{2C_V H}{\alpha}\frac{dH}{dt} \end{gathered} \tag{2.17}$$

with

$$\begin{aligned} C_V &= 0.615 - 0.201f, \quad C_Q = 0.356 - 0.273\sqrt{f}, \\ C_S &= 0.792 - 0.574\sqrt{f}, \quad C_\Upsilon = -0.034f \end{aligned} \tag{2.18}$$

where f is the dimensionless bed friction parameter $f = C_f/\alpha$. These values, obtained from fitting a large number of numerical solutions allowed for a very good representation of the swash zone properties over a wide range of H, T, α, f. By substitution of (2.18) into equation (2.16):

$$\bar{d}^3 - 2(C_V + C_\Upsilon - C_S)H^2\bar{d} - 2C_Q^2H^3 = 0 \tag{2.19}$$

Substitution for C_V, C_Q, C_S and C_Υ and solving for $\bar{d}$ gives:

$$0.45H \leq \bar{d} \leq 0.55H \quad \text{for} \quad 0 \leq f \leq 0.5 \tag{2.20}$$

If this is applied the following expressions can be used as a good approximation of the SBCs for the wave-averaged water flows:

$$\frac{dx_l}{dt} \approx R_+ - \sqrt{2gH} - \frac{4C_V}{\alpha}\frac{dH}{dt} \tag{2.21a}$$

$$\bar{d}(x_l) \approx \frac{H}{2} \tag{2.21b}$$

$$\bar{u}(x_l) \approx R_+ - \sqrt{2gH} \tag{2.21c}$$

2.2 The Modeling System

The Coupled Ocean–Atmosphere–Wave–Sediment Transport modeling system (COAWST; figure 2.1) is comprised of several components that include models for the ocean, atmosphere, surface waves, sediment transport, a coupler to exchange data fields. The COAWST modeling system includes only publicly-available components. The Model Coupling Toolkit (MCT) is the coupler used to exchange data fields between the ocean model ROMS, the atmospheric model Weather Research and Forecasting (WRF), the Simulating WAves Nearshore model (SWAN), and the sediment capabilities of the Community Sediment Transport Model. For this work, the ocean model ROMS and the wave driver SWAN have been coupled within the COAWST modeling system. In the following subsections a detailed description of MCT, SWAN and, ROMS is provided. In the ocean model, the wave fields are utilized to compute forcings in the form of radiation stress gradients that allow wave-driven flows, to compute Stokes velocities to provide correct mass flux transport, and to compute wave-enhanced bottom stresses. The wave model receives varying water levels. The ocean surface currents - velocity from the most superficial vertical-level, i.e. the cross-shore component (u_s) and the longshore component

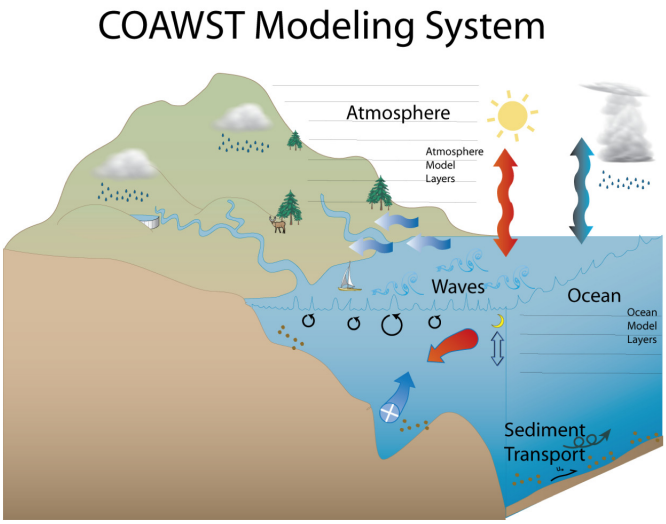

Figure 2.1: The COAWST Modeling System that joins an Ocean model, an Atmosphere model, a Waves model, and a Sediment Transport Model for studies of coastal change (`https://woodshole.er.usgs.gov/operations/modeling/COAWST`).

(v_s), affect the wave action balance by modification of the wave group celerity ($c_x + u_s, c_y + v_s$) which, in turn, affects the wave number to allow current-induced refraction.

2.2.1 The ocean model

The ocean model ROMS belongs to the general class of free surface, terrain-following numerical models that solve the three dimensional Reynolds Averaged Navier Stokes equations (RANS) using the hydrostatic and Boussinesq approximations (Shchepetkin and McWilliams 2005, 2009; Haidvogel et al. 2008) ROMS uses finite difference approximations on a horizontal curvilinear Arakawa C grid (see figure 2.2) and on a vertical stretched terrain-following coordinate. At rho-points, flow properties such as H and d are calculated, whereas at u-points and v-points, among the others, the components of the horizontal velocity and radiation stress are calculated. Momentum and scalar advection and diffusive processes

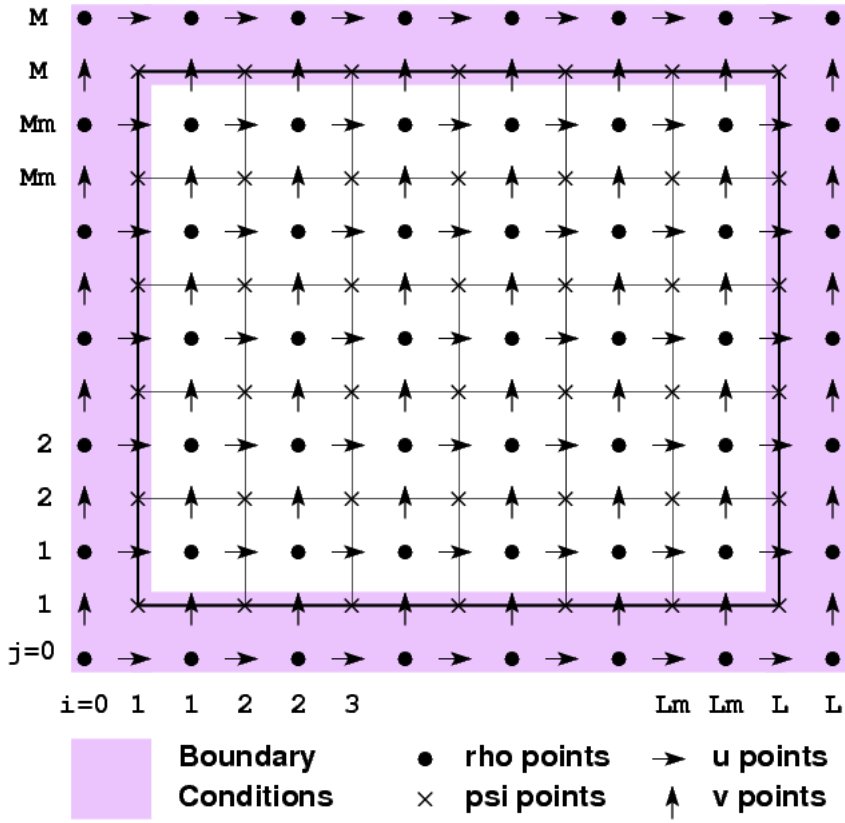

Figure 2.2: Representation of a typical ROMS grid (from Wiki ROMS).

are solved using transport equations and an equation of state computes the density field that accounts for temperature, salinity, and suspended-sediment contributions. ROMS provides a flexible structure that allows multiple choices for many of the model components, such as several options for advection schemes (second order, third order, fourth order, and positive definite), turbulence models, lateral boundary conditions, bottom- and surface-boundary layer submodels, air-sea fluxes, surface drifters, a nutrient-phytoplankton-zooplankton model, and an adjoint model for computing model inverses and data assimilation.

The hydrostatic primitive equations for momentum are solved using a split-explicit time-stepping scheme which requires special treatment and coupling between barotropic (fast) and baroclinic

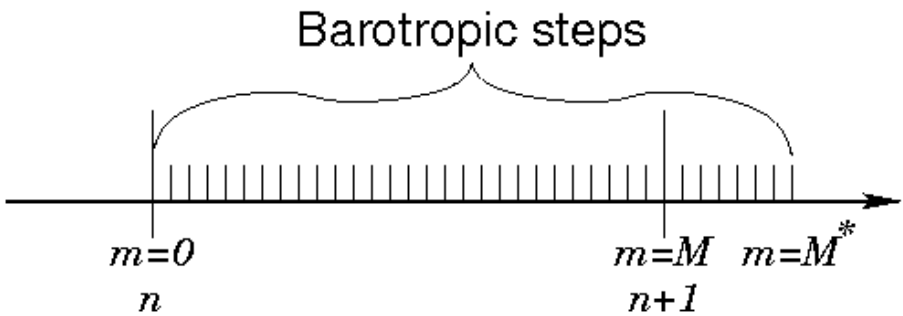

Figure 2.3: The split time stepping used in the model (Hedström 2016).

(slow) modes. A finite number of barotropic time steps (BT_{ts}), within each baroclinic time step (BT_{ts}), are carried out to evolve the free-surface and vertically integrated momentum equations. An integer ratio M between the time steps exists. In order to avoid the errors associated with the aliasing of frequencies resolved by the barotropic steps, but unresolved by the baroclinic step, the barotropic fields are time averaged before they replace those values obtained with a longer baroclinic step. Store weighted time means of the *ubar*, *vbar* fields centered at both time $n+\frac{1}{2}$ and time $n+1$ (plus the mean water elevation $\bar{\eta}$ at time $n+1$). The latter requires this time stepping to extend past time $n+1$, using M^* steps rather than just M (figure 2.3).

The model contains also a wetting and drying scheme to describe the evolution of the wave-averaged shoreline motion (Warner et al. 2013). The basic aspect of the wetting and drying algorithm is to compare the local value of the total water depth in each cell to a spatially-constant user-defined critical minimum depth (d_{crit}).

If $d < d_{crit}$, then the cell is considered to be dry and the method only prevents outward transport of volume flux from that cell. Outward transport is inhibited by forcings the magnitudes of the depth-integrated momentum terms (*ubar* and *vbar*) to be zero. Further, in a dry cell the total depth is imposed to be equal d_{crit}. Inward flux is always permitted.

The code is written in Fortran90 and runs in serial mode on a single processor, or uses either shared- or distributed-memory architectures (OpenMP or MPI) to run on multiple processors.

2.2.2 The Wave model

SWAN is a third generation spectral wave model specifically designed for shallow water that solves the spectral density evolution equation (Booij, Ris, and Holthuijsen 1999). SWAN simulates wind wave generation and propagation in coastal waters and includes the processes of refraction, diffraction, shoaling, wave–wave interactions, and dissipation due to whitecapping, wave breaking, and bottom friction. The wave model solves the action balance equation (Holthuijsen 2010):

$$\frac{\partial N}{\partial t} + \frac{\partial c_x N}{\partial x} + \frac{\partial c_y N}{\partial y} + \frac{\partial c_{\sigma N}}{\partial \sigma} + \frac{\partial c_\theta N}{\partial \theta} = \frac{S_w}{\sigma} \tag{2.22}$$

where $N(\sigma, \theta, x, y, t)$ is the action density spectrum, σ is the relative radian frequency (as observed in a frame moving with the ocean current), θ is direction normal to the wave crest, x and y are coordinate space (expressible in both spherical and Cartesian coordinates), and t is time. The action density is defined as the wave energy density E divided by the relative frequency $(N = E/\sigma)$ and is solved because the action density is conserved in the presence of currents. The group velocities in $x-$and $y-$directions c_x and c_y in the second and third terms represent the propagation of the action density in geographic space, the fourth term represents changes in relative frequency due to variations in depth and currents with a propagation speed c_σ in frequency space, and the fifth term allows depth- and current-induced refraction with a speed c_θ in directional space. The S_w term represents sources and sinks of wave energy density as described above.

2.2.3 The coupler

The coupler is the MCT (Jacob, Larson, and Ong 2005; Larson, Jacob, and Ong 2005) that allows for the transmission and transformation of various distributed data between component models using a parallel coupled approach. MCT is a program written in Fortran90 and works with the MPI communication protocol. It is compiled as a set of libraries, which are linked during the compilation.

During model initialization each model decomposes its own domain into sections (or segments) that are distributed to processors assigned for that component. Each grid section on each processor initializes into MCT, and the coupler compiles a global map to determine the distribution of model segments. Each segment also initializes an attribute vector that contains the fields to be exchanged and establishes a router to provide an exchange pathway between model components.

During the run phase of the simulation the models will reach a predetermined synchronization point, fill the attribute vectors with data, and use MCT send and receive commands to exchange fields.

2.3 SBCs implementation

The 2-D ROMS Kernel adopts a predictor-corrector numerical scheme to solve the depth-averaged continuity and momentum equations. However, for this first effort toward the implementation of the SBCs, we decided to evolve our solution only at every corrector step.

Among the ROMS variables needed to calculate the SBCs, the most important are: $\bar{u}$), d and the Vertically integrated, wave-averaged cross-shore radiation stress (hereafter S_{11}). One of the first problems to be faced for the calculation of the SBCs is that while *ubar* and d are updated at each barotropic time level, S_{11} is updated only at baroclinic time level (see section 2.2.1 for a defi-

nition of barotropic and baroclinic time levels). For this reason we decided to evolve the SBCs solution only at the first barotropic time step of each baroclinic time level. This corresponds to evolve the solution following the baroclinic time stepping. However, depth-averaged variables need boundary condition at every barotropic time step. Thus, once the SBCs values are calculated at the first barotropic time step, they are kept constant and used as boundary values for the whole baroclinic cycle (this part of the code is still not active).

Characteristic curves and positive Riemann function propagation

As shown in the set of equations (2.21), to calculate the evolution in time of x_l we need to know R_+ at x_l. This makes it necessary to propagate R_+ along the positive characteristic curves (C_+) from some chosen offshore location till x_l.

Thus, knowing the characteristic speed from equation (2.15), we thought about two different methods to calculate characteristic curves.

One is to track each C_+ from some chosen offshore point (e.g. the point where waves start breaking) to the shoreline. This means to start calculate a new C_+ at each time step and stop calculating once reached the shoreline (see figure 2.5). This introduces two problems. Since we do not know *a priori* how many time steps will be necessary for each C_+ to get to x_l, we also do not know *a priori* the number of C_+ at each time level. This means dealing with arrays with finite but indefinite dimension for which we do not know how much memory space to allocate. A possibility is to use the 'list' procedure but we disregarded this approach, because it would be too inefficient from the computational point of view. Another chance was to play with the array allocation and deallocation, which still requires a really large, though acceptable, computational effort. However, the main problem of this approach is that, at each

time step (n), the shoreward end of some C_+ characteristics, has to overlap with the position of x_l calculated at the previous time level $(n-1)$. This would hardly happen.

The other choice, which is the one used in this implementation, is to take, after very few baroclinic time step (n), x_l as the last wet point of the computational domain, (see figure 2.4). From that point, using equation (2.24), we start calculating the characteristic curves back in time, stopping after n time steps or stopping at the breaking point. Then, solving equation (2.15) we propagate along C_+ the positive Riemann variable R_+ (figure 2.6). Thus, from the time step $n+1$, the same procedure described above is repeated at the first barotropic time step of each baroclinic time level for the whole duration of the simulation but x_l and the flow property there are calculated using the set of equations (2.21).

Calculation of x_l and flow properties at x_l

Once R_+ is known at x_l the shoreline evolution can be computed using equation (2.21a). In case of positive $\frac{dx_l}{dt}$, at the first time step of a new simulation, no information is available between x_l^n and x_l^{n+1}.

From equation (2.21b) the water depth at x_l^{n+1} is known, however no information is available about $H(x_l^{n+1})$. To obtain an estimation of $H(x_l^{n+1})$, we can run the wave driver SWAN using the water depth of the present time level (n) for the wet points and setting the depth of the dry points equal the depth of the last wet point. Thus, it is possible to obtain an estimate of H^{n+1} at x_l and from equation (2.21b) also a guess of $d(x_l^{n+1})$. Now we can call iteratively SWAN, till the value of d converges. Once we have a good estimation of $d(x_l^{n+1})$, we set in ROMS $d_{crit} = d(x_l)$ and run ROMS at the next time $(n+1)$ level imposing at x_l the values of $\bar{u}$ and d calculated with equations (2.21b, 2.21c).

Albeit this approach would be probably the most precise to implement the SBC however, it would have a really high computa-

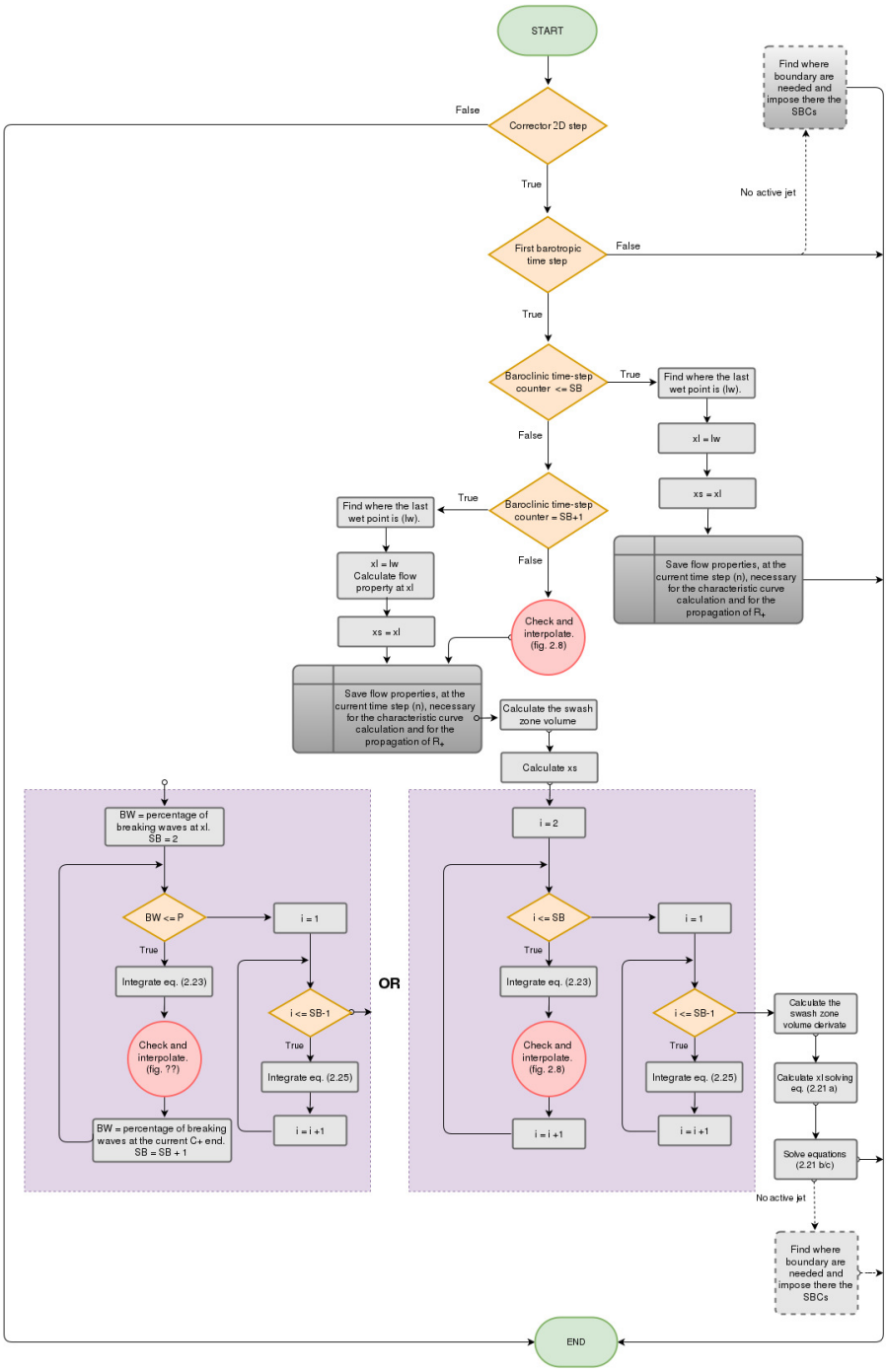

Figure 2.4: Flowchart of the embedded SBCs routine.

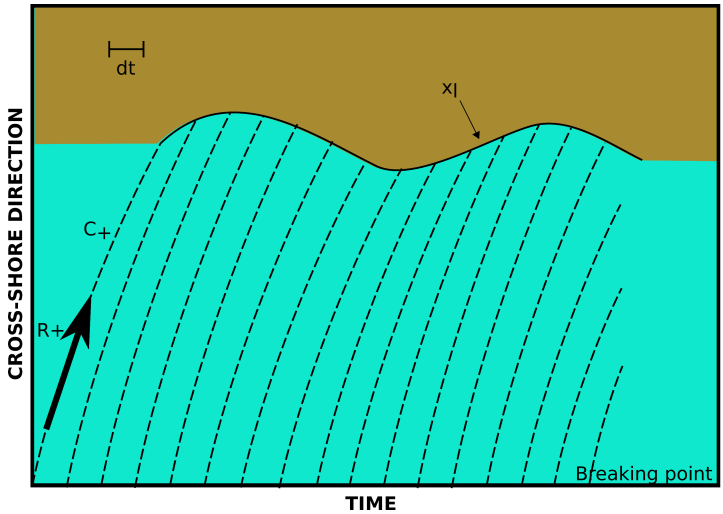

Figure 2.5: Illustration of the flow representation in the (space, time) -plane near to the shoreline. The incoming characteristic curve (C_+) carries information on the incident Riemann variable(R_+) to the mean shoreline (x_l), here taken as the envelope of the run-down positions.

tional request, it would dramatically interfere with the wetting and drying scheme, and furthermore, it would be characterized by a significant uncertainty on its convergence. We, then, opted for an approach which does not require iterations and that interferes much less with the wetting and drying algorithm. Brocchini and Peregrine (1996), proposed an approach for calculating the moving instantaneous shoreline (x_s) from the integral swash zone model. This approach assumes that the bulk of water running up and down in the swash zone is in the form of a triangular wedge (see figure 2.7). The base and the area of the triangle are known, being respectively, the water depth at x_l and the swash zone volume obtained from equation (2.17). The moving shoreline x_s can, therefore, be estimated as:

$$x_s = x_l + \frac{2\left\langle \hat{V} \right\rangle}{d(x_l)} \tag{2.23}$$

Once the x_l position is known by solving eq. (2.21a), we find where

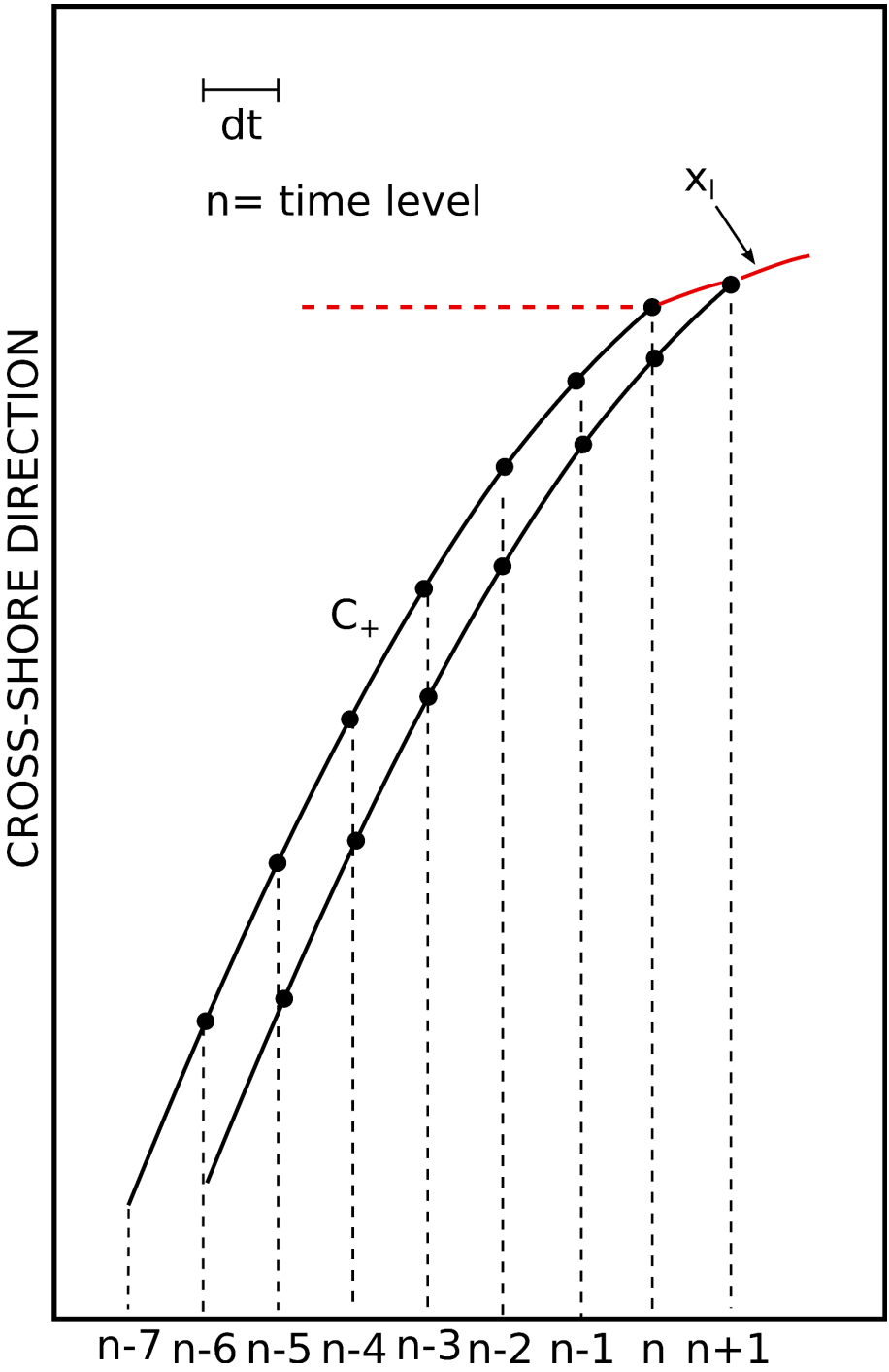

Figure 2.6: Illustration of the flow representation in the (space, time) -plane near to the shoreline. The incoming characteristic curve (C_+) carries information on the incident Riemann variable(R_+) to the mean shoreline (x_l), here taken as the envelope of the run-down positions.

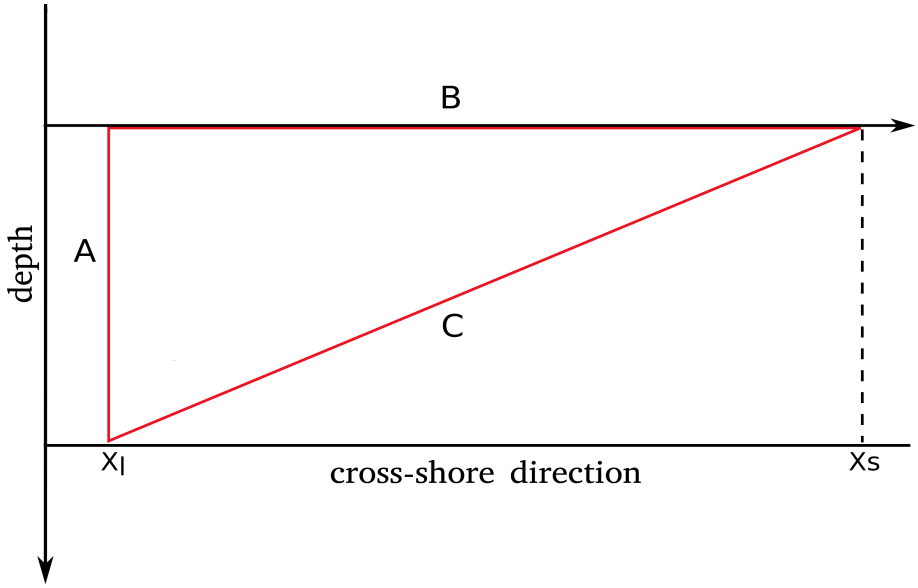

Figure 2.7: Wedge model used as simple approximation of the swash zone region. $A =$ depth at x_l, $B = \overline{x_s - x_l}$

the boundary conditions are needed (first dry point). Then we calculate the position of x_l and the values of $\bar{u}$ and d there. Further, with equation (2.23), the x_s position is calculated. The model needs boundary conditions for $\bar{u}$ and d where the first dry node lies (hereafter x_{ROMS}). Thus, there are three possibilities: x_{ROMS} lies between x_l and x_s, x_{ROMS} lies further seaward x_l or x_{ROMS} lies further shoreward x_s. In the former case, the values of $\bar{u}$ and d at x_s (where both are equal 0) and at x_l (calculated from equations 2.21b, 2.21c) are interpolated at x_{ROMS}. While in the second and third cases, the values of $\bar{u}$ and d at x_l are directly used at x_{ROMS}. This means that it is still the wetting and drying scheme to decide where the landward limit of the computational domain is but, instead of forcing $\bar{u}$ to be 0 and d to be constant, we calculate values based on the integral flow properties of the swash zone.

Interpolation of the flow properties along the Characteristic curves

When x_l is calculated from equation (2.21a) it can fall within five different wet-dry areas (see figure 2.8). For all the cases a Lagrangian interpolator with two points has been used.

1) x_l is completely surrounded by wet points (figure 2.8 case a), both rho-points (H and d) and u-points ($\bar{u}$ and S_{11}) seaward and landward x_l are wet. Flow properties at x_l are calculated by interpolating theirvalues known at the grid nodes (rho-points and u-points seaward and landward of x_l) at x_l.

2) x_l is surrounded by wet rho-points while the u-point seaward x_l is wet and the u-point landward x_l is dry (figure 2.8 case b). In this situation, H and d at x_l are retrieved the same way of the former case. For $\bar{u}$ and S_{11} a different approach is needed, since no information for these flow properties are known at the u-point landward of x_l. Here we first calculate x_s then, $\bar{u}$ and S_{11} are calculated at x_l interpolating their values from the u-point seaward x_l and of x_s where, obviously, all the flow properties, and ,thus $\bar{u}$ and S_{11}, are equal to zero.

3) x_l is surrounded by wet u-points while the rho-point seaward of x_l is wet and the rho-point landward of x_l is dry (figure 2.8 case c). In this case, $\bar{u}$ and S_{11} at x_l are calculated by interpolating there, the values of $\bar{u}$ and S_{11} from the u-points surrounding x_l. For H and d this is not possible since no information for these flow properties are known at the u-point landward of x_l. Also in this case, we first calculate x_s then, H and d are estimated at x_l by interpolating there, the values of H and d from the u-point seaward of x_l and x_s.

4) The rho-point and the u-point seaward of x_l are wet and the rho-point and the u-point landward of x_l are dry (figure 2.8 case d). All the flow properties are calculated at x_l interpolating there, their values at the rho-point and the u-point seaward of x_l and x_s.

5) x_l is completely surrounded by dry points (figure 2.8 case e).

Here the last wet point of the computational domain is first found and then used as x_l and from there C_+ is calculated. However, once equation (2.21a) is solved there, the increment in x_l is added to the last x_l calculated with the SBCs.

Once the flow property at x_l are known, equation (2.24) can be used to calculate back in time the next point of C_+ The same procedure is, then, repeated for every points along C_+ (hereafter these points are called x_c).

The numerical solution

The ROMS variables linearly interpolated along the positive characteristic curve C_+ have been used to solve the set of equations (2.21).

$$\frac{dx}{dt} = \bar{u} + c \tag{2.24}$$

where $c = \sqrt{gd}$ is the wave celerity in shallow water. A simple numerical scheme has been used to solve equation (2.15) for the propagation of R_+ along C_+. In brief, C_+ is first computed from x_l to a given offshore location (here around the breaking point). Then, along the mentioned characteristic curves the Riemann function is evolved backward from the offshore to x_l through an integration in space, rather than time (time and space are linked through 2.25): By solving equation (2.15) in its discrete form the following scheme is obtained:

$$R_{+(i+1)} = R_{+(i)} - \frac{g\alpha\Delta\ t}{(\bar{u}+c)_{i+1}} - \frac{S_{11(i+1)} - S_{11(i)}}{d_i(\bar{u}+c)_{i+1}}. \tag{2.25}$$

Once R_+ is known at x_l, having H available from the wave-driver in use, the shoreline evolution can be computed using equation (2.21a). At the lowest order of approximation the new position of the shoreline x_l^{n+1} can be obtained from:

$$x_l^{n+1} = x_l^n + \frac{dx_l}{dt}\Delta t. \tag{2.26}$$

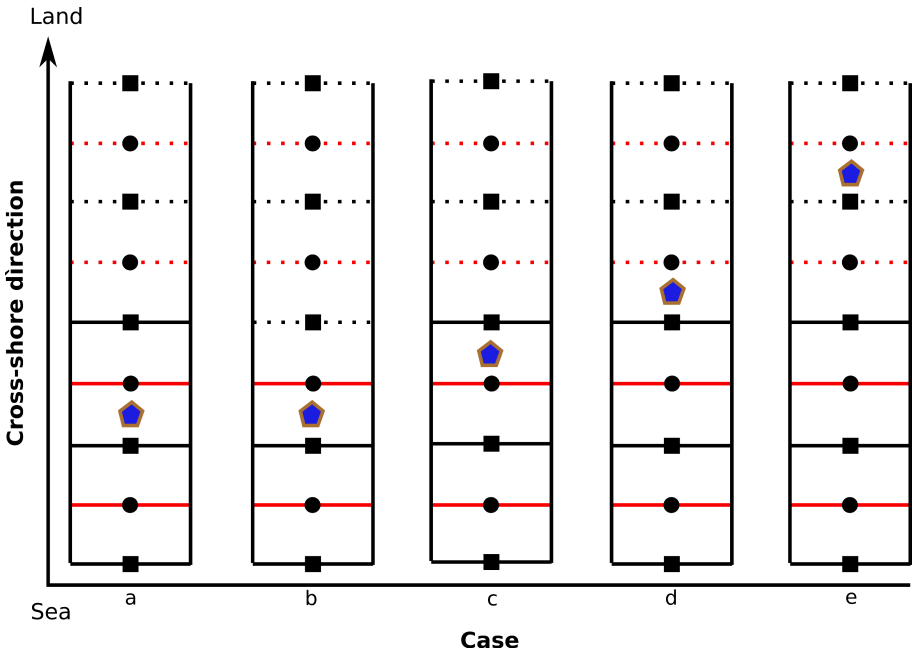

Figure 2.8: Sketch of few cross-shore sections of Arakawa-C grid with x_l (pentagon) falling in different wet-dry areas. Circles represent *rho*-points while squares represent u-points, with dotted lines indicating dry nodes and solid lines indicating wet nodes: (a) x_l completely surrounded by wet points, (b) *rho*-points and u-point seaward of x_l are wet while u-point landward of x_l is dry, (c) u-points and *rho*-point seaward of x_l are wet while the *rho*-point landward of x_l is dry, (d) *rho*- and u-points seaward of x_l are wet while both *rho*- and u-points landward of x_l are dry, (e) x_l completely surrounded by dry points.

Chapter 3

Results

3.1 Applications

3.1.1 General setup

The hydrodynamic model ROMS and the wave driver SWAN can either be run alone into the COAWST modeling system (ROMS_{sl} hereinafter) or run in conjunction with a purpose-built routine for the calculation of the mentioned SBCs (solution $\text{ROMS}_{\text{SBCs}}$ to be tested). Solutions obtained using ROMS_{sl} with a cross-shore resolution of $0.1m$, i.e. between about 120 and 170 nodes per wavelength, are used as reference solution (ROMS_{rs} hereinafter)

Grid. Test cases use spectral waves approaching a mild sloping (1/80) plane beach with a maximum depth of $1.25m$ (see Figure 3.1). Space coordinates are expressed in cartesian coordinates. The x axis points shoreward and represents the cross-shore direction while the y axis represents the long-shore direction. Grids with different cross-shore resolution have been used. To respect the Courant number condition (CFL) ($CFL < C$), when using grids with cross-shore resolution of either about 170 or 120 and 50 nodes per L_0, a baroclinic time step of $T_0/40$ or $T_0/50$ was used. Whereas, for coarser resolutions, ($L_0/24$, $L_0/12$, $L_0/6$, $L_0/3$, $L_0/2$) the baroclinic time step BC_{ts} was $T_0/4$. All the parameters for each test case are listed in Table 3.1. The results are shown in dimensionless form using T_0 for the time and the maximum off-shore

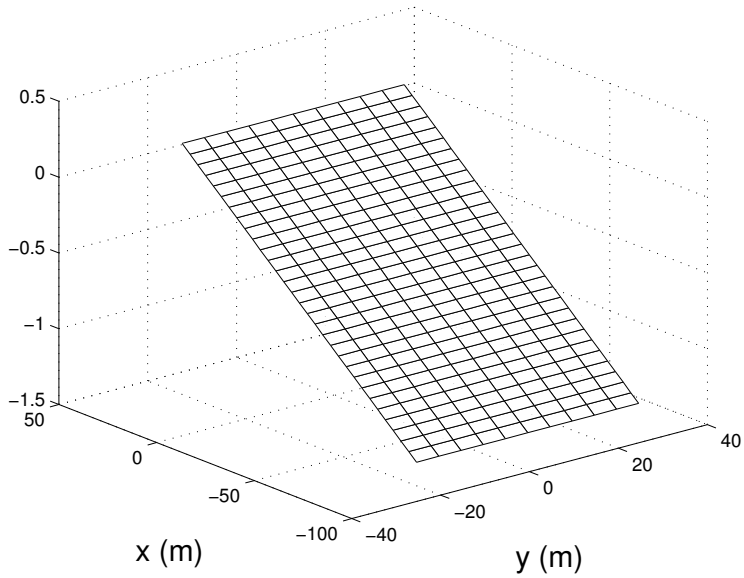

Figure 3.1: Bathymetry used for all the test cases.

wave height H_{max} for lengths.

ROMS setting. The vertical direction is discretized by eight σ levels. At the bottom a quadratic bottom friction (Chezy-type) is used. The wave fields computed from SWAN are used in ROMS to compute the radiation stress forcing. Depth-dependent radiation stress terms in the three-dimensional momentum equations and depth-indipendent radiation stress terms for the two dimensional momentum equations are calculated based on Mellor (2008). Periodic boundary condition are imposed at the lateral boundaries, for all the flows properties. At the shoreward boundary, conditions imposed by the wet and dry scheme apply, see section 2.2.1. Whereas at the seaward boundary Chapman implicit conditions are used for the free-surface and Flather conditions are used for $\bar{u}$ and $\bar{v}$ (hereafter *ubar*, *vbar*).

SWAN setting. The wave forcing is simulated with SWAN which, being a spectral model, does not allow for the generation of simple monochromatic waves. However, with the intent of better understaning the behavior of the SBCs, we try to have a wave field

Table 3.1: Model parameters for the three test cases

Models parameter	Test case 1	Test case 2	Test case 3
Length (cross-shore)	120 m	120 m	120 m
Width (longshore)	50 m	50 m	50 m
Duration	20 min	1 hour	20 min
Offshore incident wave period (T_0)	5 s	4 s	4 s
Offshore wave direction	0°	0°	0°
Bottom stress formulation	Quadratic	Quadratic	Quadratic
Friction factor	0.005	0.005	0.005
Bottom roughness	0.015 m	0.015 m	0.015 m
Off-shore depth (d_0)	1.25 m	1.25 m	1.25 m
Off-shore wave length L_0	16.9 m	11.8 m	11.8 m
Critical depth $dcrit$	0.001 m	0.001 m	0.001 m
Coupling time	1 s	1 s	1 s
Swan time step	1 s	1 s	1 s
Baroclinic time step (BC_{ts})	1 s	1 s	1 s
Barotropic time step (BT_{ts})	$BC_{ts}/30$	$BC_{ts}/30$	$BC_{ts}/30$

as close as possible to a monochromatic wave field by focussing the energy in one frequency bin. See table 3.1 for details about wave heights and peak periods used. SWAN was configured to use 36 directional bins and 11 frequency bins between $0.01T_0$ and $0.25T_0$ with T_0 representing the off-shore input wave period. Incoming waves propagating perpendicular to the coast enter the computational domain throughout the offshore boundary while at the shoreward boundary, perfect absorption of the energy left is imposed. Periodic boundary condition are used at the two domain boundaries parallel to the cross-shore direction.

3.1.2 Test case 1

For this test case, an incoming wave with height H_0 of about $d_0/5$ was used (figure 3.2 top-left panel) with a $L_0/170$ cross-shore resolution. Steady-state conditions have been reached after 2 minutes of run, i.e. after about 24 T_0 the cross-shore profiles of setup (figure 3.2 top-right panel), wave height (figure 3.2 bottom-left panel) and cross-shore current (figure 3.2 bottom-right panel) became con-

stant.

The H began to decrease near $x = -50m$ due to wave breaking dissipation. Not surprising for a wave-averaged model, forcing the simulation with a constant H_0 leads to a constant wave setup shoreward. Figure 3.3 represents the evolution of the shore-

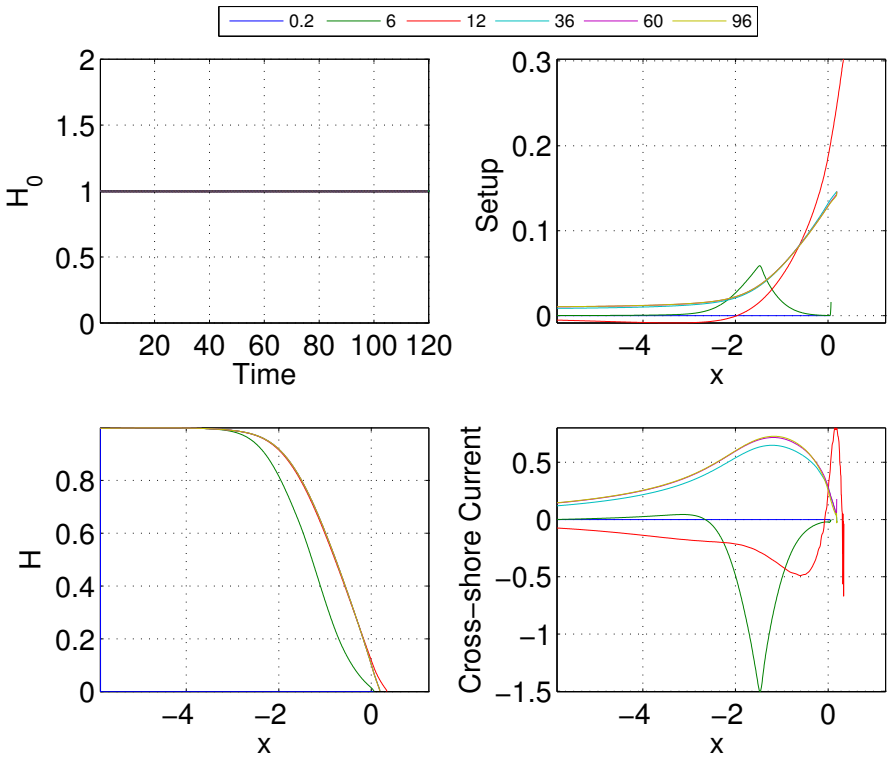

Figure 3.2: Dimensionless results for Test case 1: evolution of H_0 at the offshore boundary (top-left panel); mid domain cross-shore section at different times of: wave setup (top-right panel), H (bottom-left panel) and *ubar* (bottom-right panel).

line (x_l) respectively computed with ROMS_{rs} and $\text{ROMS}_{\text{SBCs}}$. The two solutions are pretty similar however, the shoreline obtained with $\text{ROMS}_{\text{SBCs}}$ is spatially shifted shoreward of about 30 cm, i.e. about 10% of the maximum runup to steady conditions, and time shifted of few seconds (i.e. some T_0). After an initial large run-up and then run-down, the mean shoreline reaches a steady state. The shoreline position is given by integration of equation (2.21a). Fig-

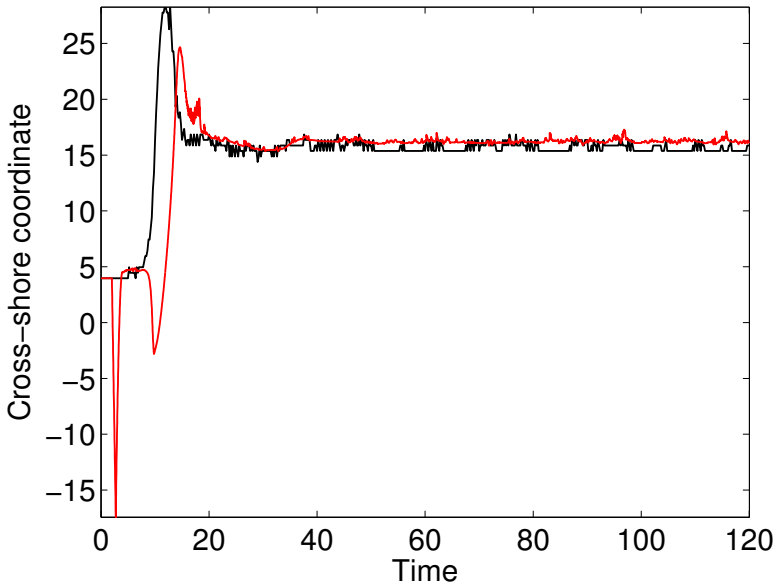

Figure 3.3: Shoreline (dimensionless) evolution for the first 10 minutes of runs with a $L_0/170$ cross-shore resolution. The black line represents x_l computed with $\mathrm{ROMS_{rs}}$, while the red line gives x_l computed with $\mathrm{ROMS_{SBCs}}$.

ure 3.4 shows how to the initial run-up and run-down corresponds respectively, an increase of all terms of the right-hand side of equation (2.21a), followed by a decrease of all the terms. In figure 3.5 the black lines represent the characteristic curves calculated from the integration of equation (2.24). Characteristic curves have been calculated at each baroclinic time step (BT_{ts}) however, for the sake of clarity, they are plotted in figure 3.5 only every second.

3.1.3 Test case 2

The second test case, consists of a wave train with a off-shore wave height (H_0) given by:

$$H_0 = H_{max} - \left| \frac{H_{max}}{T_{tr}/2} t - H_{max} \right|_n \tag{3.1}$$

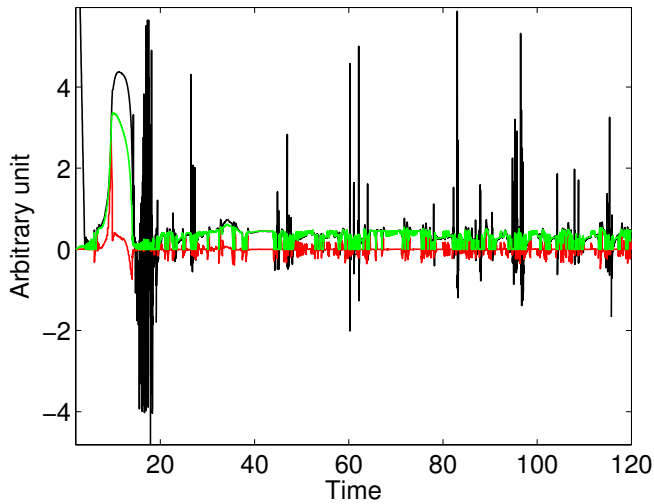

Figure 3.4: Evolution at x_l of the right-hand side terms of equation (2.21a), in dimensionless form: first term (black line), second term (red line), and third term (green line).

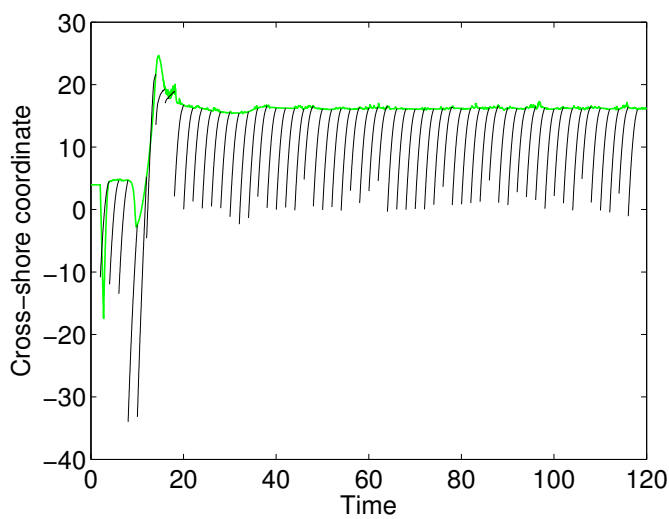

Figure 3.5: Shoreline (dimensionless) evolution for the first 10 minutes of run (about 120 input periods) with a $L_0/170$ cross-shore resolution (green line) and characteristic curves (equation 2.24; black lines).

where T_{tr} is the wave train period, t is the time (second) and n is the number of wave trains entering the computational domain along the off-shore boundary (see figure 3.6 top-left panel). For this test case $H_{max} = d_0/5$ was used with $T_{tr} = 30\,T_0$, $0 \leq t \leq 120$ and $n = duration/T_{tr}$. The purpose here is to generate a low frequency signal to simulate an oscillation of the shoreline and test till which cross-shore resolution it is possible to reproduce x_l with both $\mathrm{ROMS_{sl}}$ and $\mathrm{ROMS_{SBCs}}$.

Grids with different cross-shore resolutions, ranging from about 120 to 1.5 nodes per L_0, have been used. Moving toward coarser resolutions we expect to loose the shoreline signal when $\mathrm{ROMS_{sl}}$ is used. Whereas, running $\mathrm{ROMS_{SBCs}}$, we expect to be still able to reproduce x_l.

Also in this case, the steady-state (in a statistical sense) condition, has been reached after 2 minutes of run (i.e. after 24 T_0). This becomes evident observing the cross-shore profile of the setup (figure 3.6 top-right panel), H_0 (figure 3.6 bottom-left panel) and cross-shore current (figure 3.6 bottom-right panel). From the second minute, the same pattern is repeated with period T_{tr}. The mean shorelines computed at several cross-shore resolutions with both $\mathrm{ROMS_{sl}}$ and $\mathrm{ROMS_{SBCs}}$ are shown in figure 3.7. At really high cross-shore resolution both $\mathrm{ROMS_{sl}}$ and $\mathrm{ROMS_{SBCs}}$, reproduce x_l in a similar fashion.

However, using $\mathrm{ROMS_{sl}}$ with an increasingly coarse cross-shore resolution, leads to a rapid loss of the shoreline signal. The same is not true for the shoreline calculated with $\mathrm{ROMS_{SBCs}}$, which is well resolved up to a 8.0 m (about half L_0) cross-shore resolutions, when x_l starts to be distorted. It is also to be noted that, going towards coarser resolutions, the shoreline calculated by $\mathrm{ROMS_{sl}}$ moves landward while that computed by $\mathrm{ROMS_{SBCs}}$ oscillates over the same spatial range of the well-resolved case. In figure 3.8 the same simulations are represented for the last 10 minutes of the simulations. For the $L_0/120$ and $L_0/50$ onshore resolutions, the two solutions of x_l overlap when the shoreline moves landward. However, the

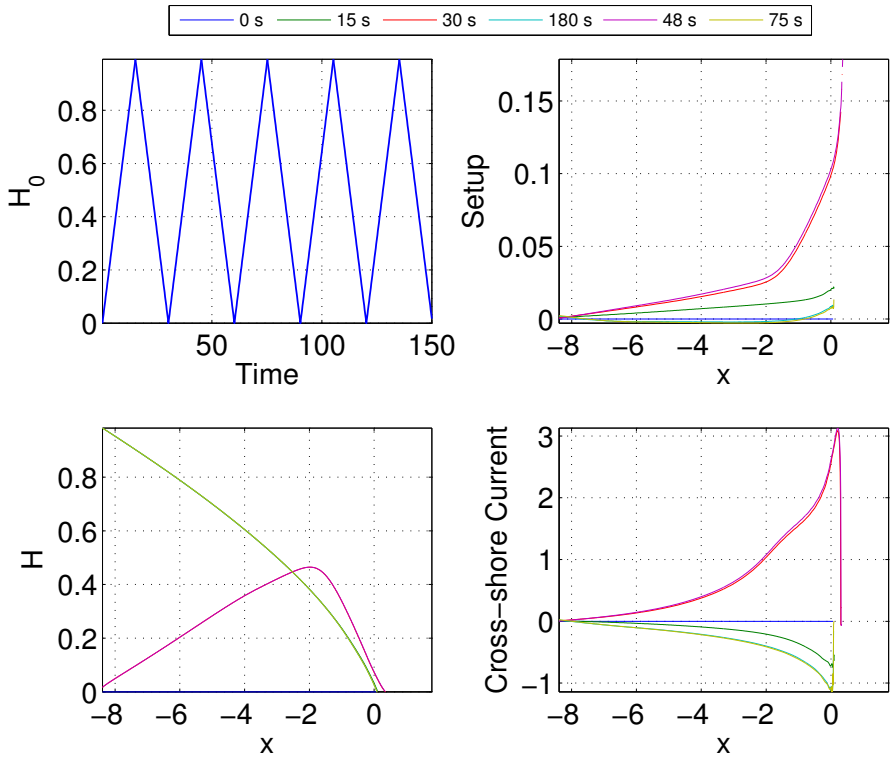

Figure 3.6: Dimensionless results for Test case 2: evolution of H_0 at the offshore boundary (top-left panel); cross-shore section at different times of: wave setup (top-right panel), H (bottom-left panel) and *ubar* (bottom-right panel).

shoreline computed with $\text{ROMS}_{\text{SBCs}}$ has a crest further landward compared with the shoreline computed with ROMS_{sl}. The same is true when the shoreline moves seaward and for the shoreline trough. With increasing grid size, the shoreline computed with $\text{ROMS}_{\text{SBCs}}$ keeps oscillating around the well-resolved mean shoreline, while the ROMS_{sl} shoreline significantly migrates shoreward and increases in width. The mean shorelines computed with $\text{ROMS}_{\text{SBCs}}$ at the different onshore resolution, are compared with the one obtained with the well-resolved ROMS_{rs} in figure 3.9. The $\text{ROMS}_{\text{SBCs}}$ solutions are really similar to ROMS_{rs} solution up to 8.0 m (about half L_0) cross-shore resolution where the two shorelines behave in a very different way.

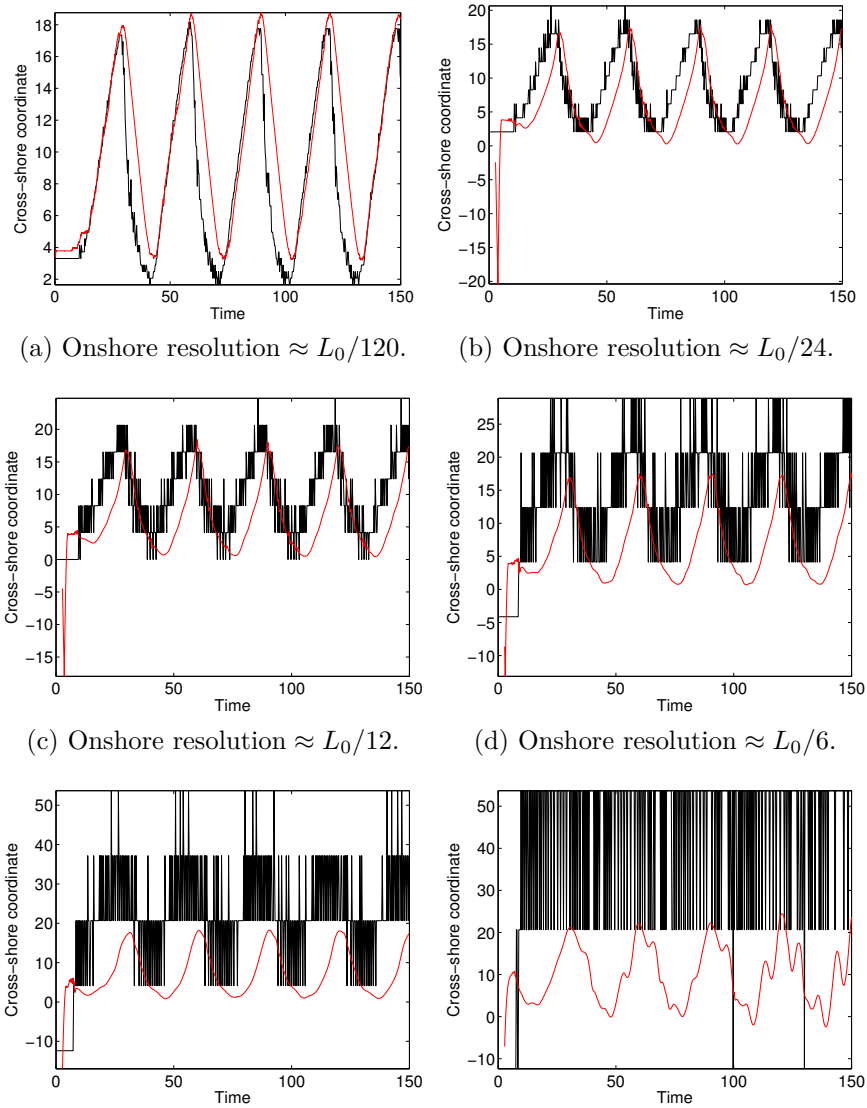

(a) Onshore resolution $\approx L_0/120$.

(b) Onshore resolution $\approx L_0/24$.

(c) Onshore resolution $\approx L_0/12$.

(d) Onshore resolution $\approx L_0/6$.

(e) Onshore resolution $\approx L_0/3$.

(f) Onshore resolution $\approx L_0/2$.

Figure 3.7: Dimensionless results for test case 2: shoreline evolution for the first 10 minutes of run (about 5 T_{tr}) using grids with different cross-shore resolution. The black lines represents x_l computed with ROMS_{sl}, while the red lines give x_l computed with $\text{ROMS}_{\text{SBCs}}$.

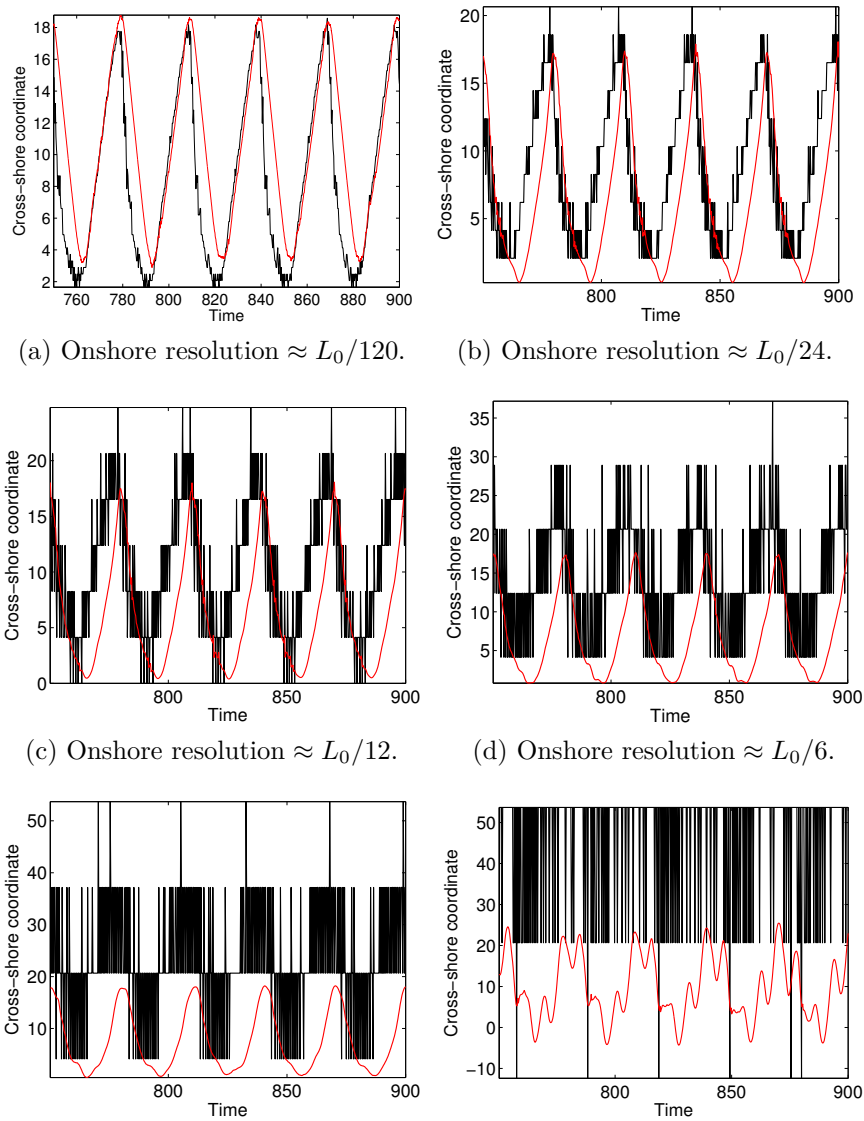

(a) Onshore resolution $\approx L_0/120$.

(b) Onshore resolution $\approx L_0/24$.

(c) Onshore resolution $\approx L_0/12$.

(d) Onshore resolution $\approx L_0/6$.

(e) Onshore resolution $\approx L_0/3$.

(f) Onshore resolution $\approx L_0/2$.

Figure 3.8: Dimensionless results for test case 2: shoreline evolution for the last 10 minutes of run (about 5 T_{tr}) using grids with different cross-shore resolution. The black lines represent x_l computed with $\mathrm{ROMS_{sl}}$, while the red lines give x_l computed with $\mathrm{ROMS_{SBCs}}$.

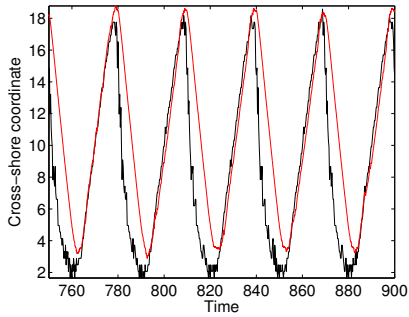

(a) Onshore resolution $\approx L_0/120$.

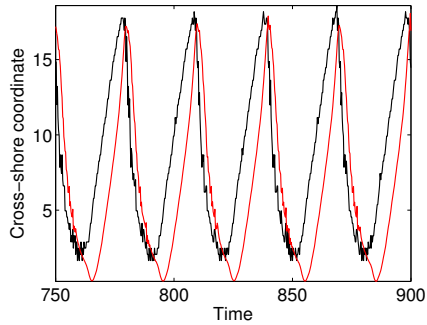

(b) Onshore resolution $\approx L_0/24$.

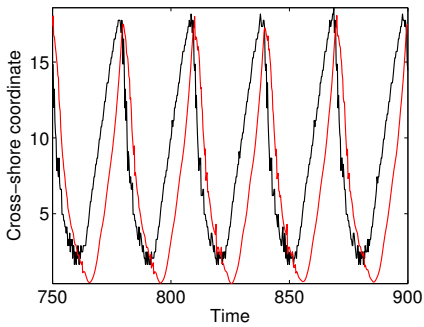

(c) Onshore resolution $\approx L_0/12$.

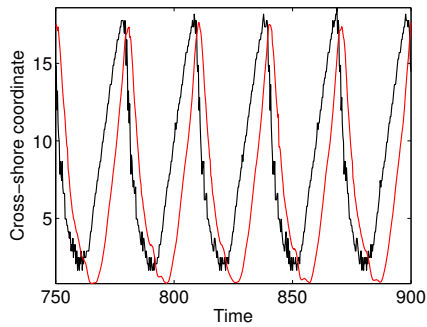

(d) Onshore resolution $\approx L_o/6$.

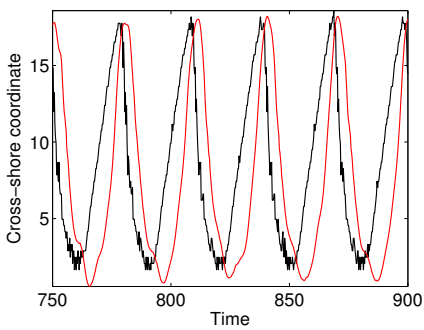

(e) Onshore resolution $\approx L_0/3$.

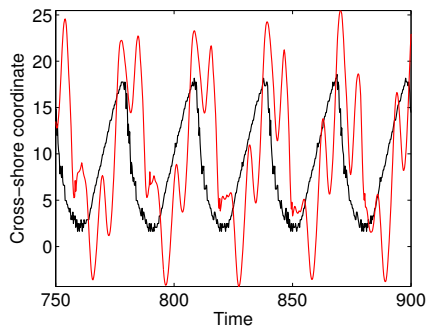

(f) Onshore resolution $\approx L_0/2$.

Figure 3.9: Dimensionless results for test case 2: shoreline evolution for the last 10 minutes of run (about 5 T_{tr}) using grids with different cross-shore resolution. The black lines represent x_l computed with $\mathrm{ROMS_{rs}}$, while the red lines give x_l computed with $\mathrm{ROMS_{SBCs}}$.

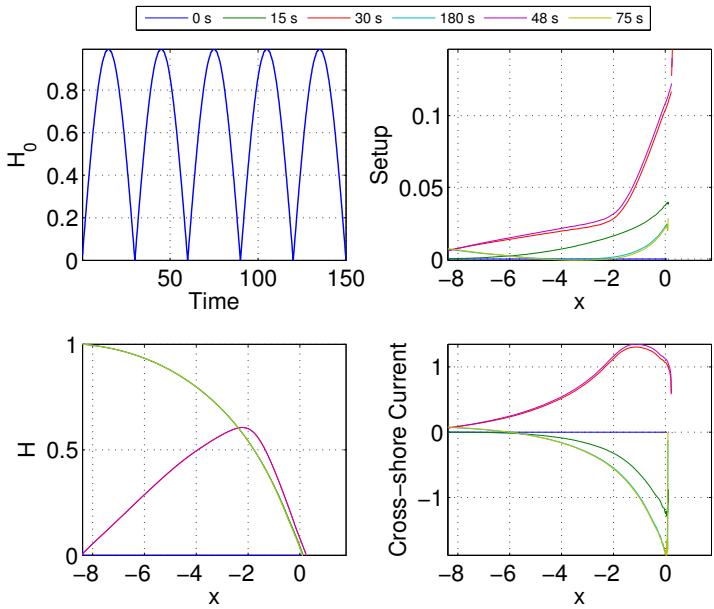

Figure 3.10: Dimensionless results for Test case 3: evolution of H_0 at the offshore boundary (top-left panel); cross-shore section at different times of: wave setup (top-right panel), H (bottom-left panel) and *ubar* (bottom-right panel).

3.1.4 Test case 3

The final test case, consists of a wave train with a H_0 given by:

$$H_0 = H_{max} \left| \sin \frac{2\pi}{T_{tr}} t \right| \tag{3.2}$$

where T_{tr} is still the wave train period and t is the time). For this test case $H_{max} = d_0/5$ and $T_{tr} = 30\,T_0$ (see figure 3.10 top-left panel). In this case, the purpose is try to understand the causes of the distortion of the x_l signal when runs are carried with $\text{ROMS}_{\text{SBCs}}$ on the grid with 8.0 m (about half wavelength) cross-shore resolution. Grids with different cross-shore resolutions, ranging from about $L_0/120$ to about $L_0/2$, have been used.

Again, the steady-state (in a statistical sense) condition, has been reached after 24 T_0 of run (see figure 3.10). In figure 3.11 and figure 3.12, the mean shorelines are illustrated, respectively, at the

beginning and at the end of the simulations. Whereas in figure 3.13 the shoreline solutions obtained with $\mathrm{ROMS_{SBCs}}$ are compared with the ones from $\mathrm{ROMS_{rs}}$. Results are pretty similar to the ones of test case 2. However, here the shoreline excursion is smaller due to the lower H_{max} and the shoreline crests are wider because the wave height changes as a sine function. The characteristic curves, calculated from the integration of equation (2.24) within a time-interval of $2.5T_0$, are shown in figure 3.14. Characteristic curves have been calculated at each baroclinic time step however, for the sake clarity, they are plotted only every 2.5 times of T_0.

Inspection of the shape of the characteristic curves, for resolutions from about $L_0/120$ to about $L_0/3$, reveals that while the characteristic speeds of the incoming characteristics are almost constant, those of the outgoing characteristics are not. Different is the situation with resolution of $L_0/2$ where, under the extra crest of the distorted x_l, some characteristic curves become almost parallel to the abscissa axis with a consequent characteristic speeds close to zero. The three terms of the right-hand side of equation (2.21a) are shown for all the simulations in figure 3.14. From fine to coarser resolutions, the first and the second term of equation (2.21a) increase their magnitude. The same is not true for the third term which remains unchanged. As expected, their period reflects T_{tr}, except for the simulation with resolution of $L_0/2$ which has higher frequency. Contour maps of near shoreline depth, from $\mathrm{ROMS_{rs}}$ and from $\mathrm{ROMS_{SBCs}}$ at resolutions $L_0/12$ $L_0/3$ $L_0/2$, are shown in figure 3.16. Depth is well represented by $\mathrm{ROMS_{SBCs}}$ up to the resolution $L_0/2$ where it is not properly represented anymore. However the near shoreline depth computed with $\mathrm{ROMS_{SBCs}}$ is slightly deeper during the rundown and slightly more shallow in the runup. This is due to the time shift between the two solutions. Contour maps of near shoreline cross-shore velocity for the two solutions are represented in figure 3.17. For this flow property, the two solution obtained with $\mathrm{ROMS_{rs}}$ and $\mathrm{ROMS_{SBCs}}$ are not reallyclose anymore.

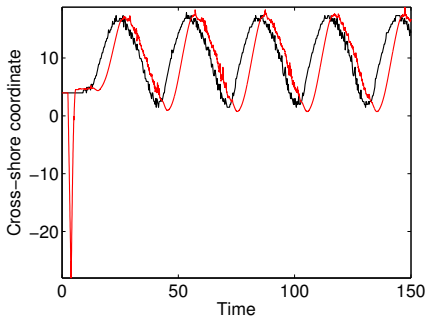

(a) Onshore resolution $\approx L_0/120$.

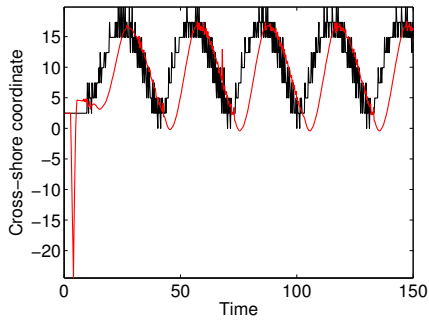

(b) Onshore resolution $\approx L_0/24$.

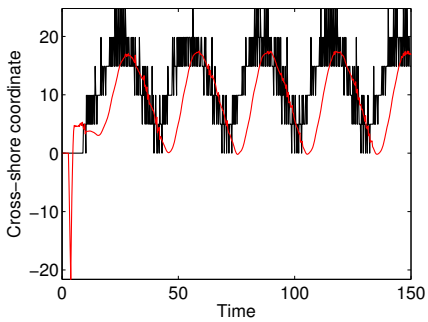

(c) Onshore resolution $\approx L_0/12$.

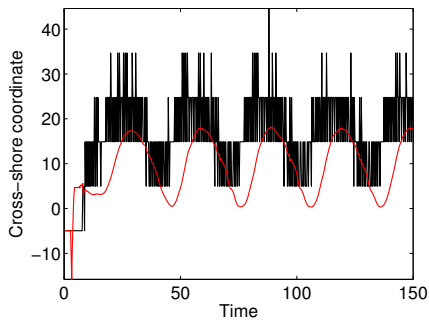

(d) Onshore resolution $\approx L_0/6$.

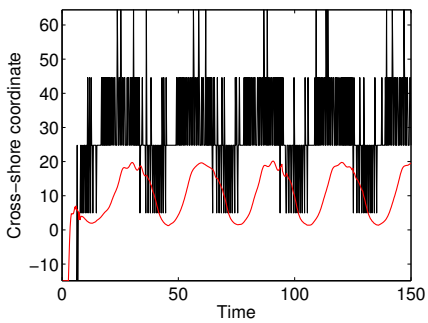

(e) Onshore resolution $\approx L_0/3$.

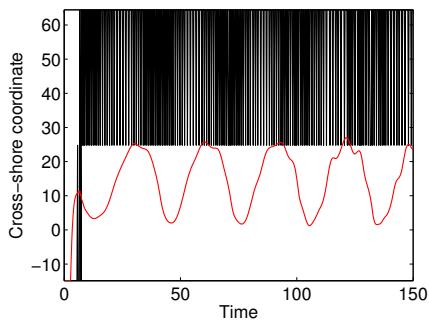

(f) Onshore resolution $\approx L_0/2$.

Figure 3.11: Dimensionless results for Test case 3: shoreline evolution for the first 10 minutes of run (about 5 T_{tr}) using grids with different cross-shore resolution. The black lines represents x_l computed with ROMS_{sl}, while the red lines give x_l computed with $\text{ROMS}_{\text{SBCs}}$.

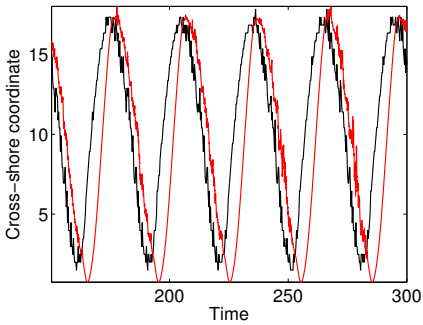

(a) Onshore resolution $\approx L_0/120$.

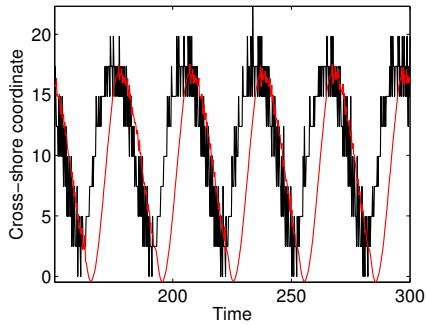

(b) Onshore resolution $\approx L_0/24$.

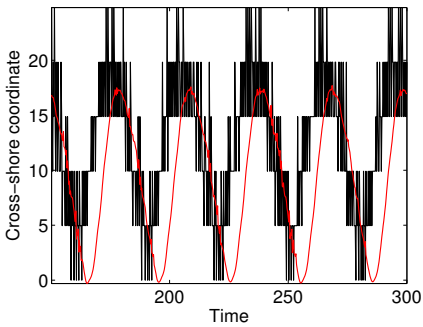

(c) Onshore resolution $\approx L_0/12$.

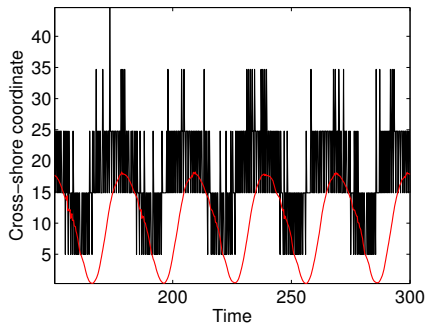

(d) Onshore resolution $\approx L_0/6$.

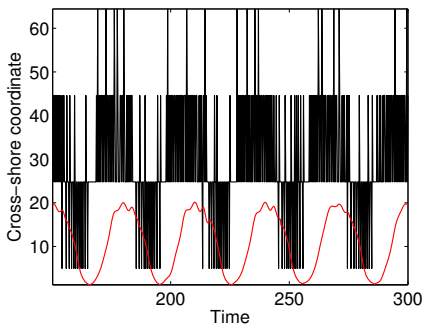

(e) Onshore resolution $\approx L_0/3$.

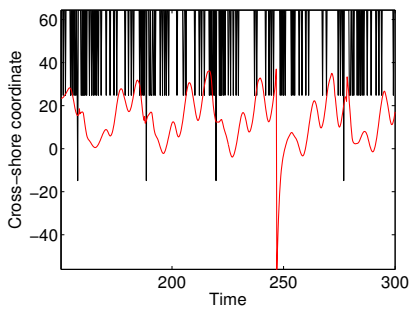

(f) Onshore resolution $\approx L_0/2$.

Figure 3.12: Dimensionless results for Test case 3: shoreline evolution for the last 10 minutes of run (about 5 T_{tr}) using grids with different cross-shore resolution. The black lines represent x_l computed with ROMS_{sl}, while the red lines give x_l computed with $\text{ROMS}_{\text{SBCs}}$.

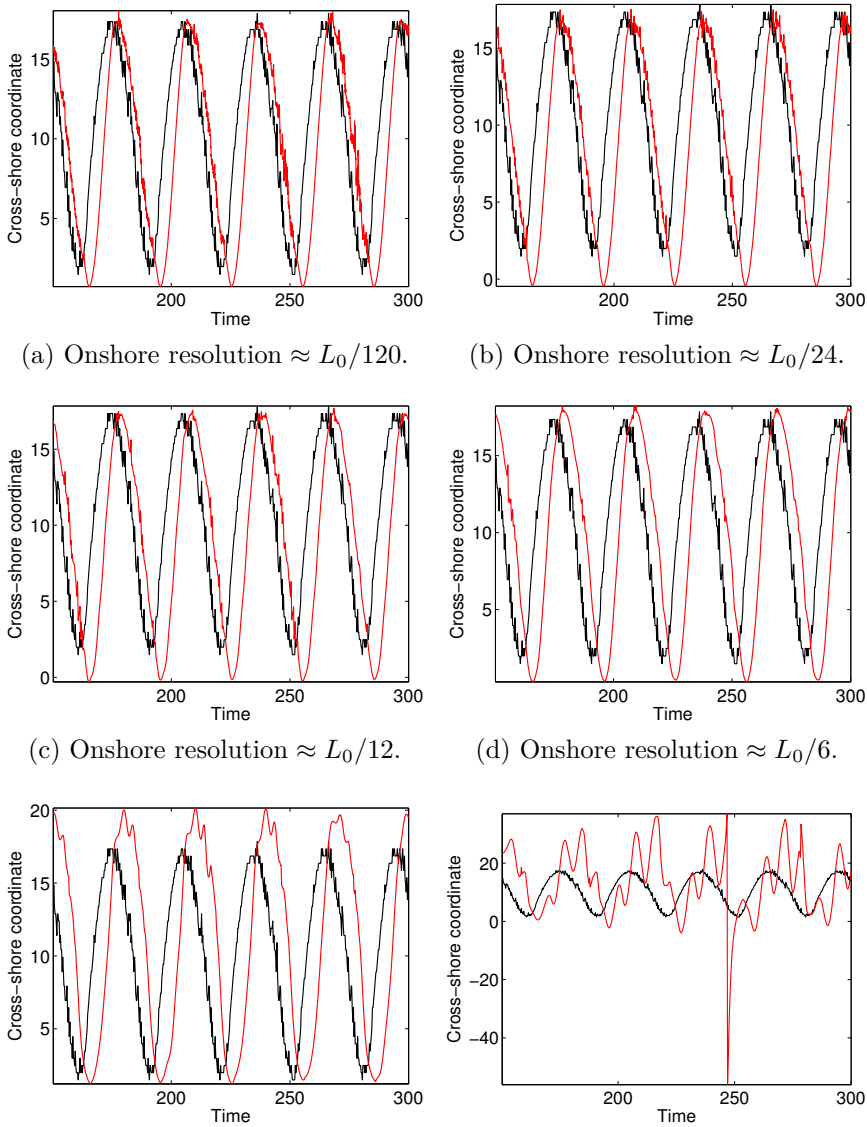

(a) Onshore resolution $\approx L_0/120$.

(b) Onshore resolution $\approx L_0/24$.

(c) Onshore resolution $\approx L_0/12$.

(d) Onshore resolution $\approx L_0/6$.

(e) Onshore resolution $\approx L_0/3$.

(f) Onshore resolution $\approx L_0/2$.

Figure 3.13: Dimensionless results for Test case 3: shoreline evolution for the last 10 minutes of run (about 5 T_{tr}) using grids with different cross-shore resolution. The black lines represent x_l computed with $\mathrm{ROMS_{rs}}$, while the red lines give x_l computed with $\mathrm{ROMS_{SBCs}}$.

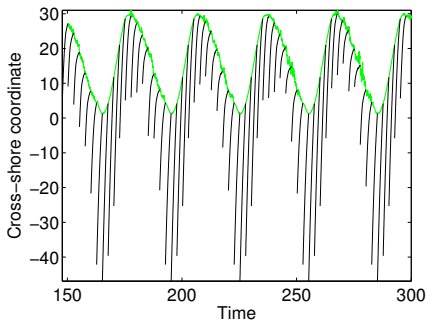

(a) Onshore resolution $\approx L_0/120$.

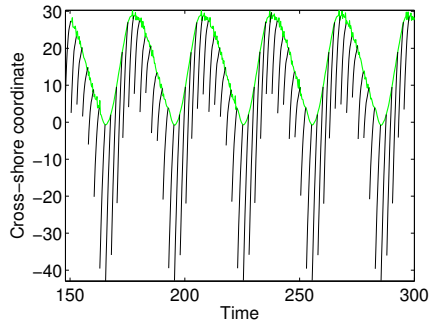

(b) Onshore resolution $\approx L_0/24$.

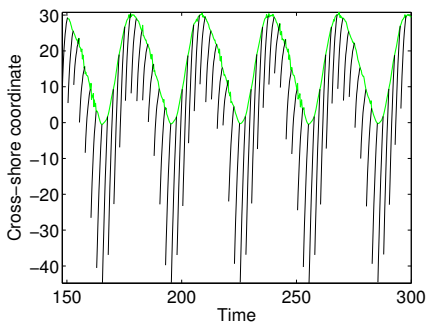

(c) Onshore resolution $\approx L_0/12$.

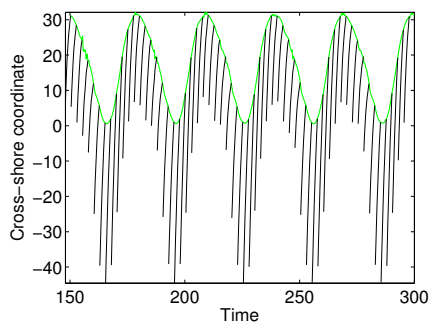

(d) Onshore resolution $\approx L_0/6$.

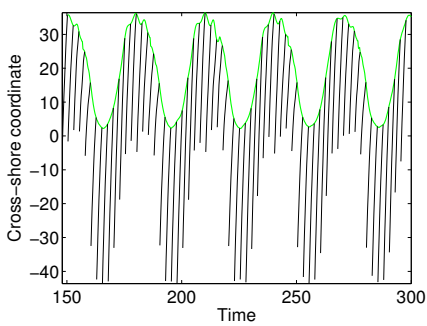

(e) Onshore resolution $\approx L_0/3$.

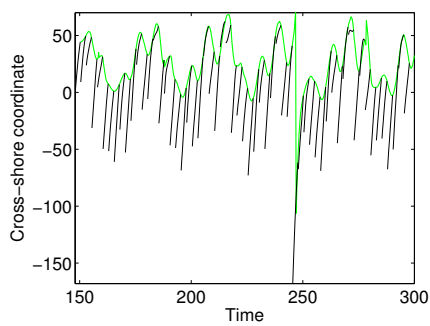

(f) Onshore resolution $\approx L_0/2$.

Figure 3.14: Dimensionless results for Test case 3: shoreline evolution for the last 10 minutes of run (about 5 T_{tr}; green line) and characteristic curves below it (equation 2.24; black lines).

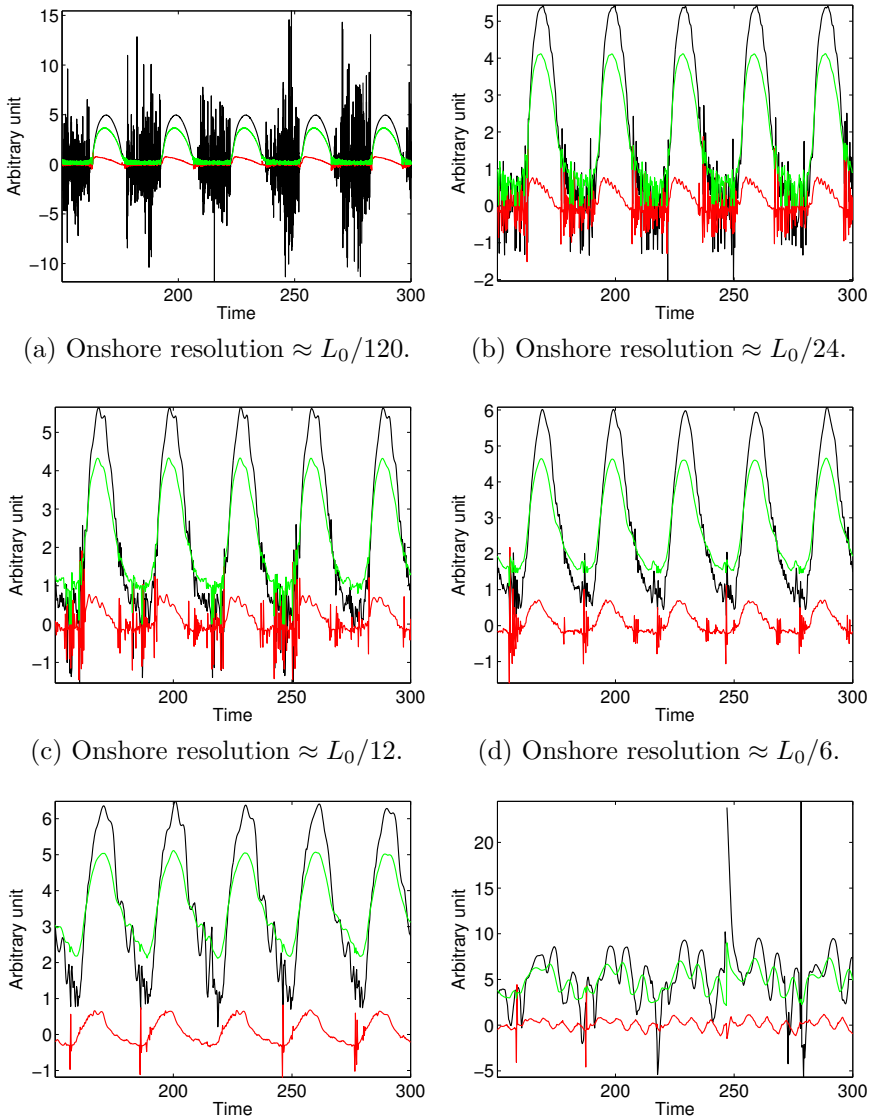

(a) Onshore resolution $\approx L_0/120$.

(b) Onshore resolution $\approx L_0/24$.

(c) Onshore resolution $\approx L_0/12$.

(d) Onshore resolution $\approx L_0/6$.

(e) Onshore resolution $\approx L_0/3$.

(f) Onshore resolution $\approx L_0/2$.

Figure 3.15: Dimensionless results for Test case 3: evolution at x_l of the right-hand side terms of equation (2.21a): first term (black line), second term (green line), and third term (red line).

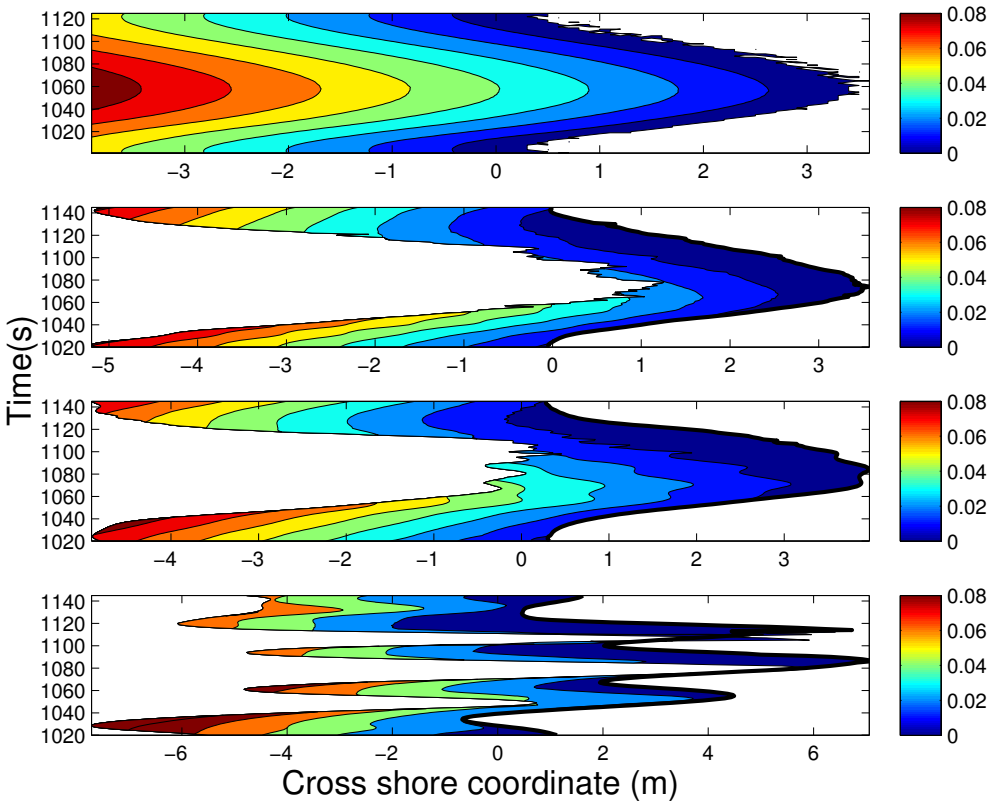

Figure 3.16: Results for Test case 3: near shoreline depth. Solution obtained with (from the top to the bottom): $\mathrm{ROMS_{rs}}$, $\mathrm{ROMS_{SBCs}}$ with $L_0/12$, $\mathrm{ROMS_{SBCs}}$ with $L_0/3$ and $\mathrm{ROMS_{SBCs}}$ with $L_0/2$.

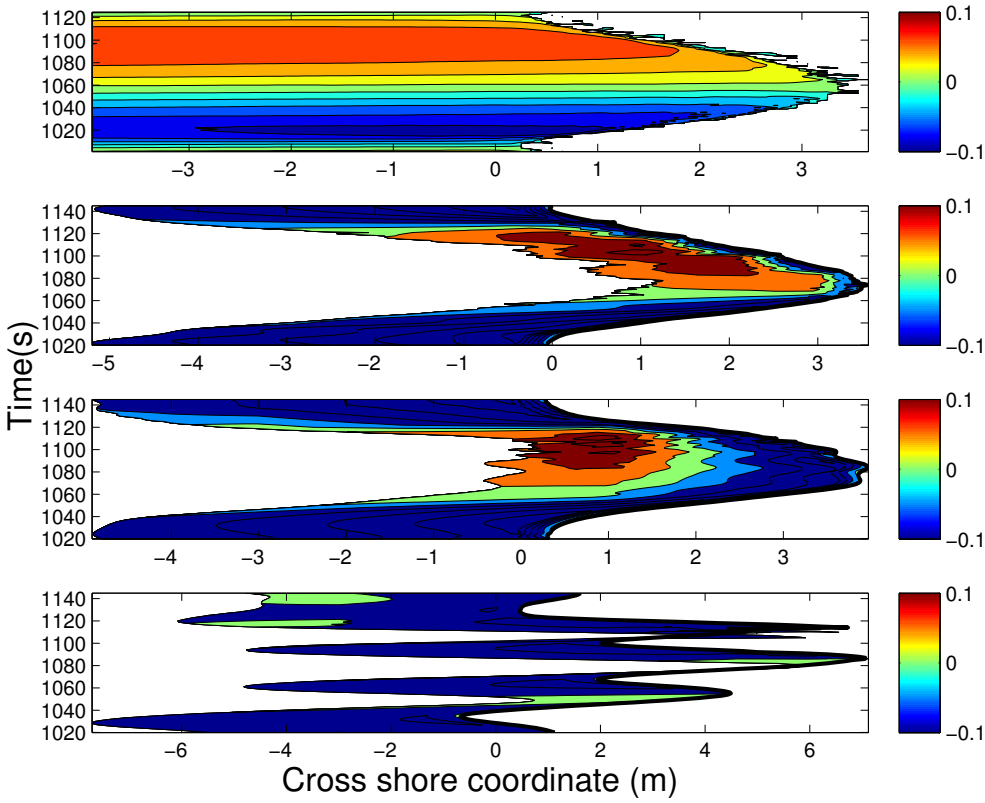

Figure 3.17: Results for Test case 3: near shoreline cross-shore velocity. Solution obtained with (from the top to the bottom): $\mathrm{ROMS_{rs}}$, $\mathrm{ROMS_{SBCs}}$ with $L_0/12$, $\mathrm{ROMS_{SBCs}}$ with $L_0/3$ and $\mathrm{ROMS_{SBCs}}$ with $L_0/2$.

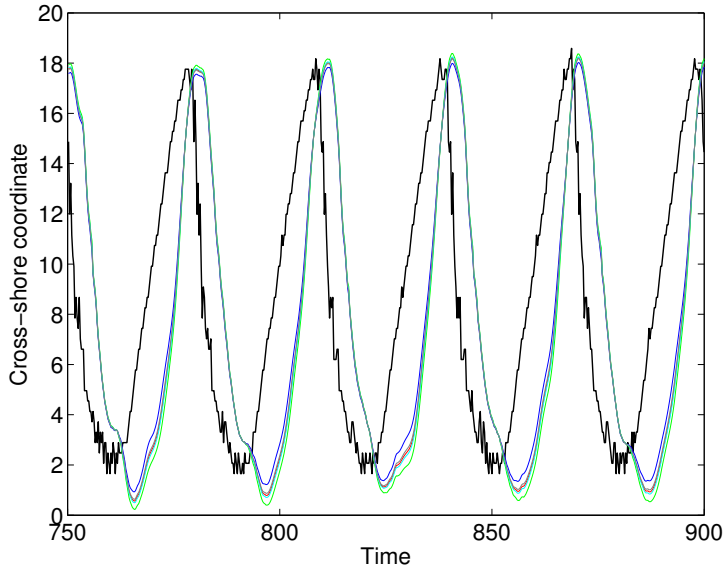

Figure 3.18: Sensitivity analysis for the function Cv. The black line represents x_l dimensionless computed with $\mathrm{ROMS_{rs}}$, while the other lines represent the dimensionless shorelines obtained with $\mathrm{ROMS_{SBCs}}$ using different values for Cv. Red line: $Cv = 0.615 - 0.201f$, blue line: $Cv = 0.400 - 0.201f$, green line: $Cv = 0.800 - 201f$, cyan line: $Cv = 0.615 - 0.101f$, grey line: $Cv = 0.615 - 0.301f$.

3.2 Parametric analyses

In this section, results of a sensitivity analysis on few parameters of interest are shown. All the simulations presented here, have been forced by incoming wave trains with a H_0 given by equation (3.1), $H_{max} \approx 1/5$ of the offshore water depth was used, $T_{tr} = 30\,T_0$, i.e. $0 \leq t \leq T_{tr}$ and $n = duration/T_{tr}$. The grid resolution was always $L_0/3$.

Results of the sensitivity analysis on the function C_v are reported in figure 3.18. From such results, the function C_v does not seems to play a crucial role for the calculation of the mean shoreline. However, a weak effect of Cv, can be observed especially around the shoreline trough. In order to estimate the effect of the swash zone volume in the calculation of the shoreline, equation (2.21a) was

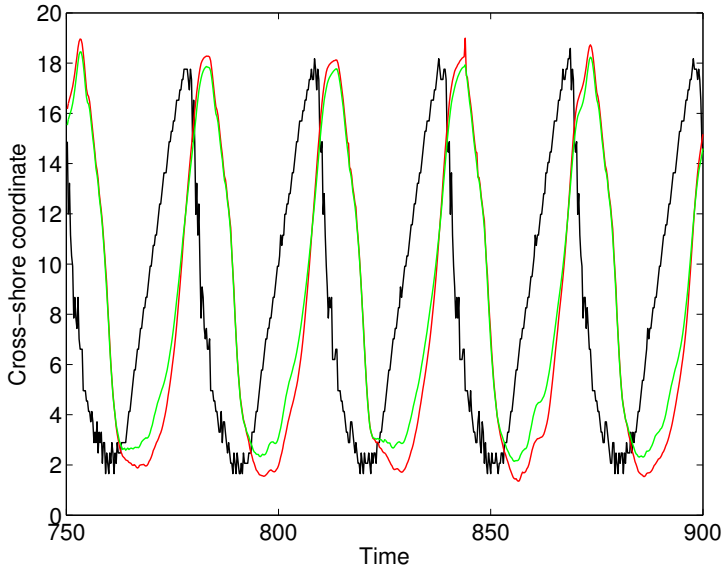

Figure 3.19: Dimensionless shoreline evolution for the last 10 minutes of run (about 5 T_{tr}). The black line is x_l obtained with $\mathrm{ROMS_{rs}}$, the red line is x_l obtained with $\mathrm{ROMS_{SBCs}}$ and the green line is x_l obtained with $\mathrm{ROMS_{SBCs}}$ excluding the third term of equation (2.21a).

solved excluding the third term of the right-hand side. Comparison of the obtained shoreline with that obtained with $\mathrm{ROMS_{rs}}$ and the one with $\mathrm{ROMS_{SBCs}}$ when resolving the full version of equation (2.21a) is shown in figure 3.19.

Like for the Cv parameter, at least for the present test case, we observe no significant effect in the calculation of x_l due to the swash zone volume. Nevertheless, also in this case, some evident effects of the absence of the swash zone volume, are shown by an alteration of the shoreline trough shape.

Sensitivity analyses have been carried out also to test the best location where to start the integration of R_+. For this purpose, the code was modified in order to define as the starting point for the propagation of R_+, the point where at least a given percentage of waves started breaking, rather than in terms of a given distance from the shoreline. This methodology having a clear physical

meaning since the wave breaking phenomena largely influences the energy that reaches the shoreline.

Results of the sensitivity analysis on R_+ (figures 3.20, 3.21 and 3.22) suggest the starting point for the integration of R_+ as a crucial element for the calculation of the mean shoreline. Looking at the results of (figure 3.20), it appears evident that the best location where to start the propagation of R_+ is where 5% of the waves start to break.

3.3 Fourier analysis

The x_l signals of the third test case have been decomposed in its basic components by applying the Discrete Fourier Transform (DFT). The DFT was computed using a Fast Fourier Transform (FFT) algorithm within the matlab environment. The sampling frequency (fs) was enough to largely satisfy the sampling theorem (Shannon 1949), which establishes a sufficient condition for the sampling frequency, in order to well reproduce the information from a continuous-time signal. The sampling theorem states that $fs > 2 * fm$ where fm is the bandwidth limit of the signal.

The amplitude of the basic components are given by the module of the complex series coefficients c_n. Fourier transform results for the shoreline calculated with $\mathrm{ROMS_{rs}}$ are shown in the bottom panel of figure 3.23. There are three peaks characterizing the spectrum, one of these should be the shoreline frequency itself. The same frequencies distribution are found also when x_l is computed by $\mathrm{ROMS_{SBCs}}$ with a cross-shore resolution of $L_0/120$ (figure 3.24), $L_0/12$ (figure 3.25) up to $L_0/3$ (figure 3.26). Different is the situation for the shoreline computed with $\mathrm{ROMS_{SBCs}}$ at a resolution of $L_0/2$ (figure 3.27), which is characterized by a broader frequency band that includes higher frequencies than the other resolutions.

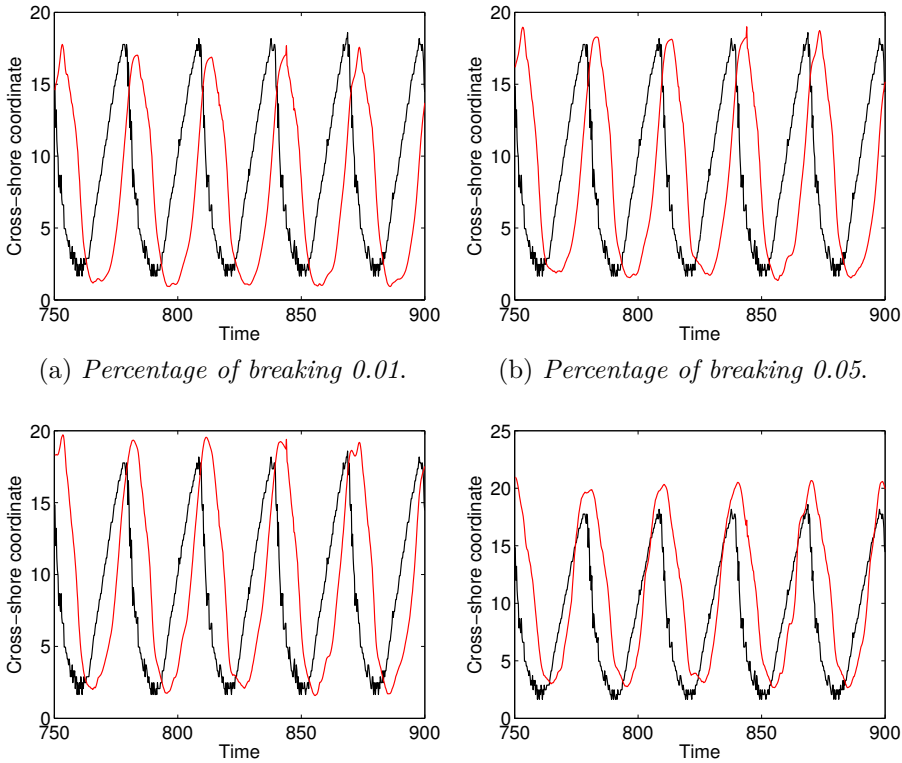

(a) *Percentage of breaking 0.01.*

(b) *Percentage of breaking 0.05.*

(c) *Percentage of breaking 0.10.*

(d) *Percentage of breaking 0.50.*

Figure 3.20: Dimensionless results of the sensitivity analysis on the starting point for the propagation of R_+. Shoreline evolution for the last 10 minutes of run (about 5 T_{tr}) using different starting points for the propagation of R_+. The black lines represent x_l computed with$\mathrm{ROMS_{rl}}$, while the red lines give x_l computed with$\mathrm{ROMS_{SBCs}}$.

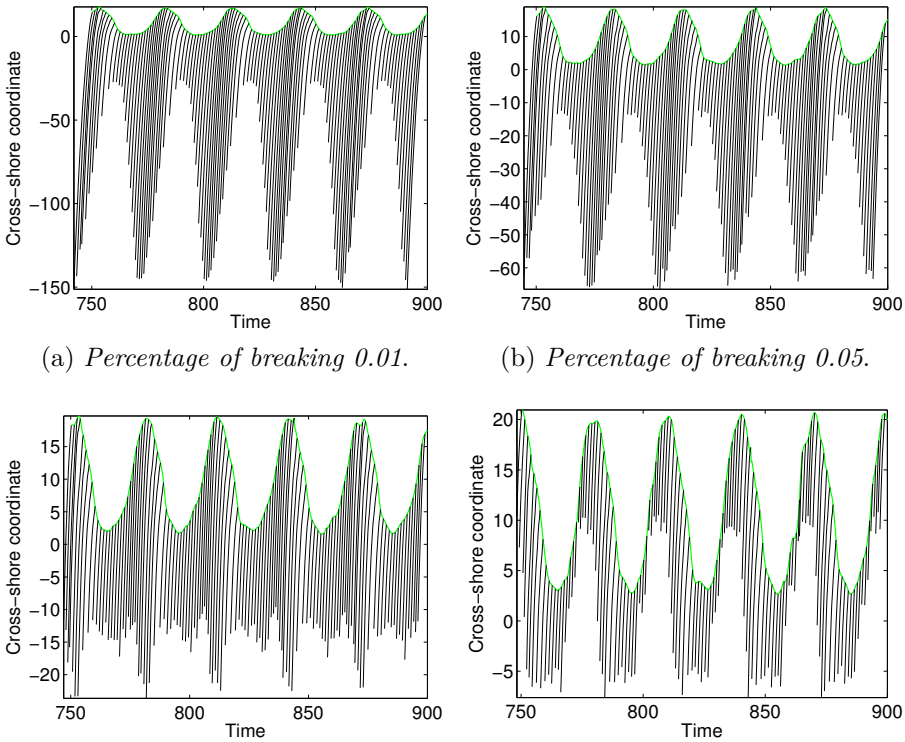

(a) *Percentage of breaking 0.01.*

(b) *Percentage of breaking 0.05.*

(c) *Percentage of breaking 0.10.*

(d) *Percentage of breaking 0.50.*

Figure 3.21: Dimensionless results of the sensitivity analysis on the starting point for the propagation of R_+. Shoreline evolution for the last 10 minutes of run (about 5 T_{tr}; green line) and incoming characteristic curves (equation 2.24; black lines).

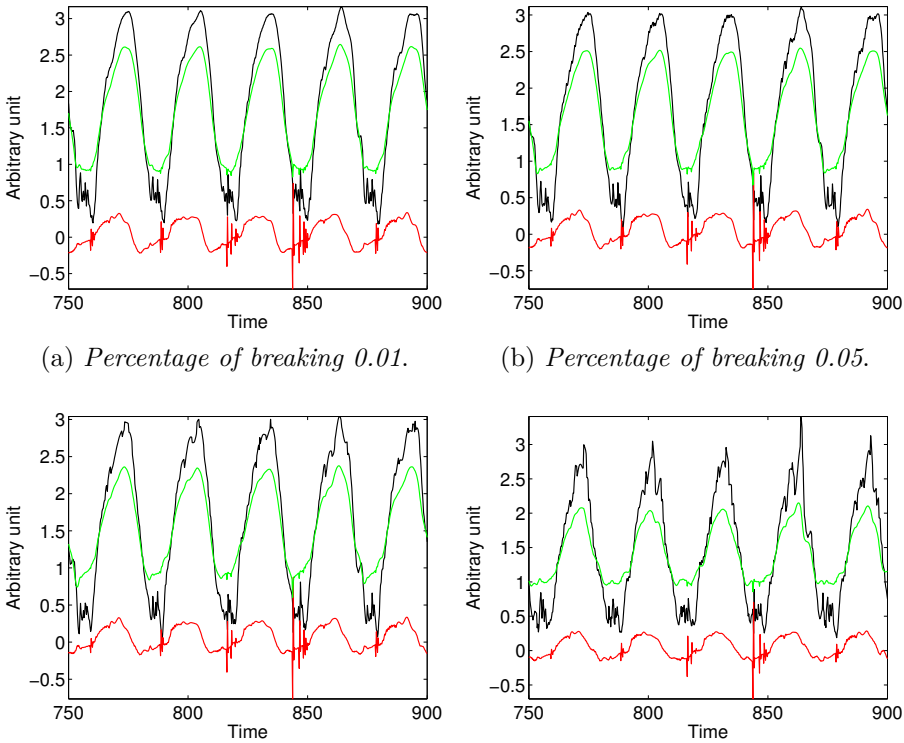

(a) *Percentage of breaking 0.01.*

(b) *Percentage of breaking 0.05.*

(c) *Percentage of breaking 0.10.*

(d) *Percentage of breaking 0.50.*

Figure 3.22: Dimensionless results of the sensitivity analysis on the starting point for the propagation of R_+. Evolution at x_l of the right-hand side terms of equation (2.21a): first term (black line), second term (green line), and third term (red line).

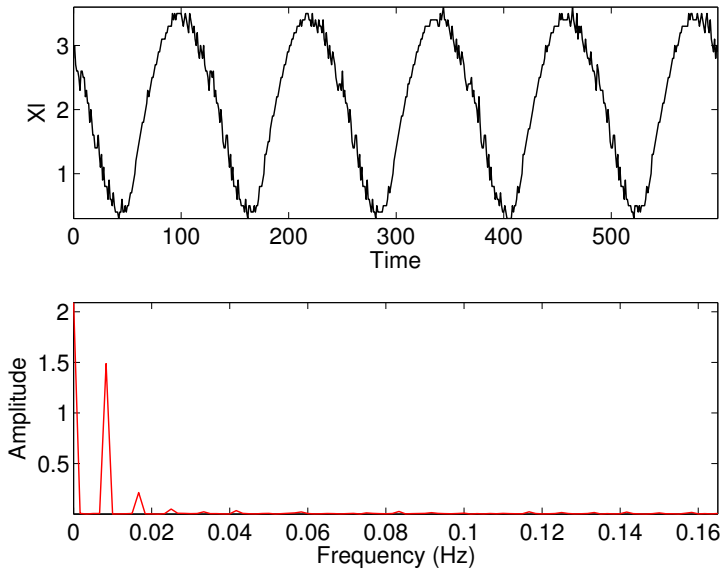

Figure 3.23: Fourier analysis results. x_l from $\mathrm{ROMS_{rs}}$ (top panel) and its Fourier transform (bottom panel).

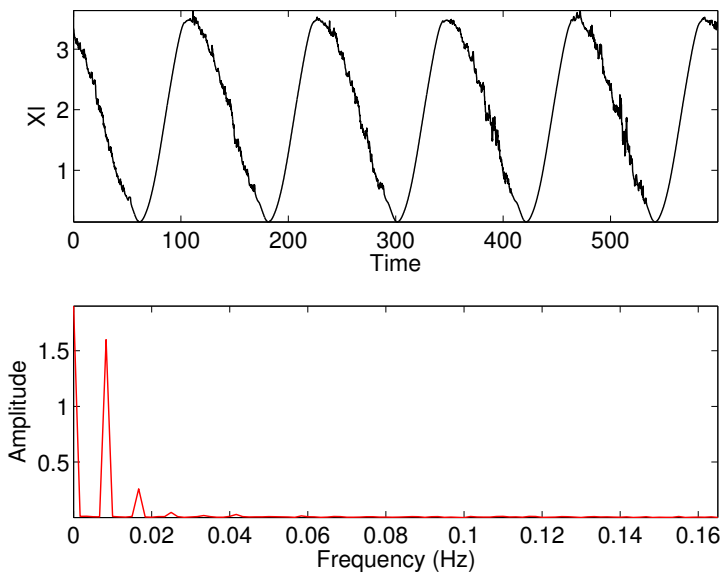

Figure 3.24: Fourier analysis results. x_l from $\mathrm{ROMS_{SBCs}}$ with a cross-shore resolution of $L_0/120$ (top panel) and its Fourier transform (bottom panel).

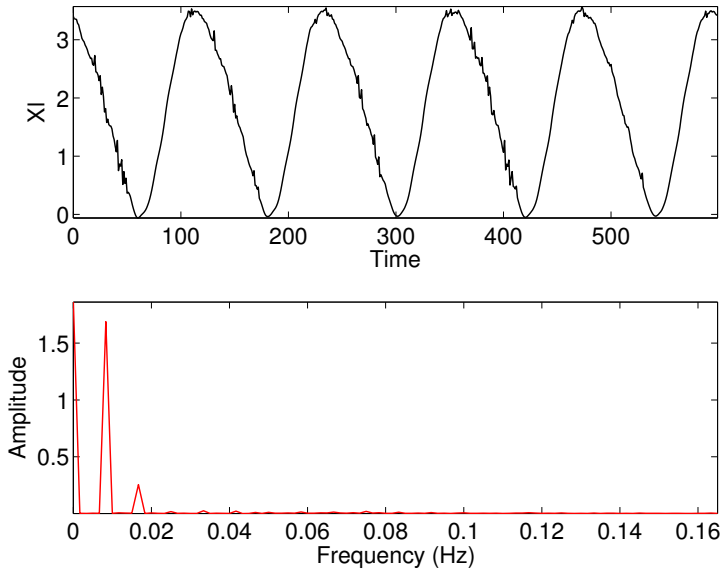

Figure 3.25: Fourier analysis results. x_l from ROMS$_{\text{SBCs}}$ with a cross-shore resolution of $L_0/12$ (top panel) and its Fourier transform (bottom panel).

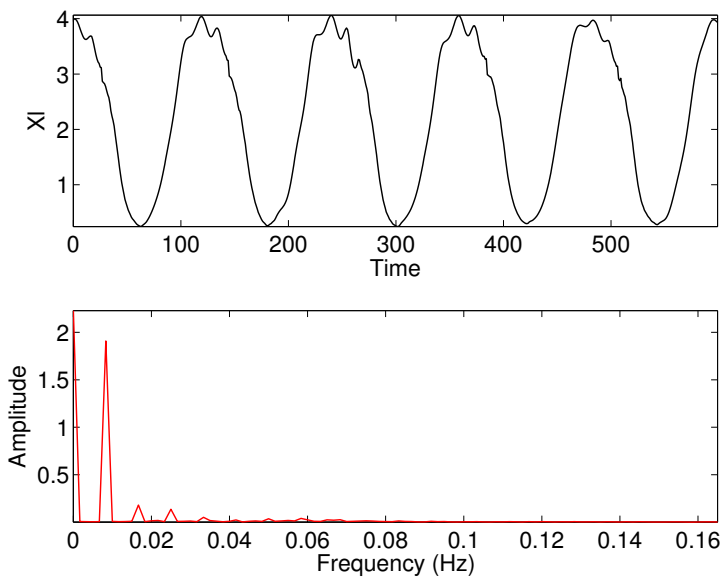

Figure 3.26: Fourier analysis results. x_l from ROMS$_{\text{SBCs}}$ with a cross-shore resolution of $L_0/3$ (top panel) and its fourier transform (bottom panel).

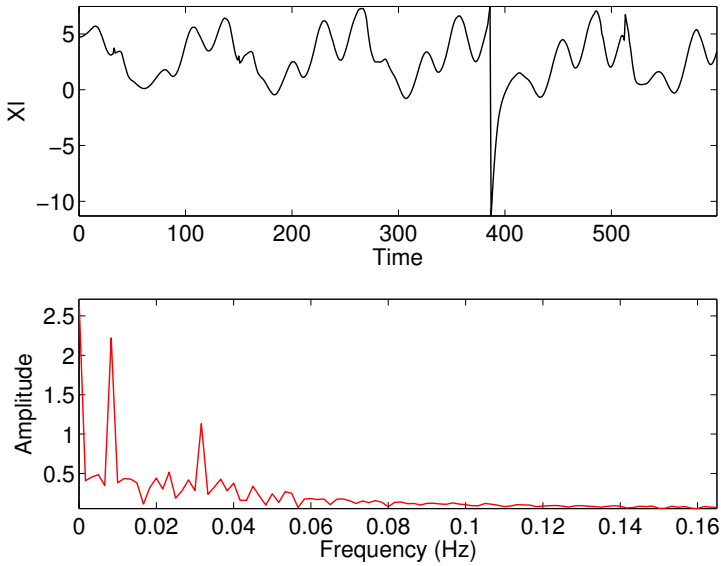

Figure 3.27: Fourier analysis results. x_l from ROMS$_{\text{SBCs}}$ with a cross-shore resolution of $L_0/2$ (top panel) and its Fourier transform (bottom panel).

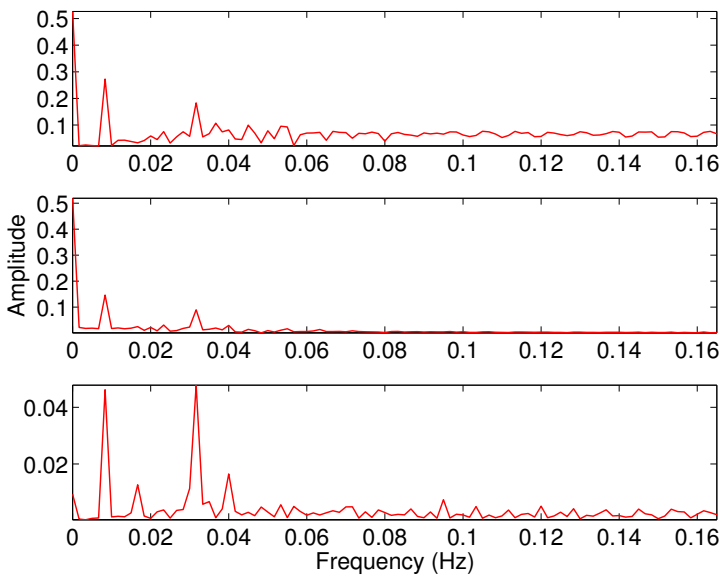

Figure 3.28: Fourier analysis results. The three terms of the right hand side of equation (2.21a) from ROMS$_{\text{SBCs}}$ with a cross-shore resolution of $L_0/2$. First term (top panel), second term (middle panel) and third term (bottom panel).

Chapter 4

Discussion

4.1 Integral model validation

The proposed new SBSs have been included in ROMS as a purpose-builtin routine. When using grids with cross-shore resolution of about 170 nodes per wavelength together with a really small *dcrit* (see section 2.2.1; in this work a *dcrit* of 0.001 m was always used) it is possible to solve the equations of motion and the continuity equation in very shallow water, i.e. up to the shoreline. In this condition, the model does not need any external boundary conditions to represent the swash zone since the fluid properties are calculated in there. Further, the small *dcrit* used is very close to 0, where the artificial shoreline conditions of rigid wall describe well the shoreline motion. Such simulations are really time consuming and computational effort requiring. Thus, they are not useful from a practical point of view. However, running ROMS in these conditions ($\mathrm{ROMS_{rs}}$) allowed us to compute a benchmark solution to assess the value of the proposes SBSs.

Test case 1

Already from test case 1, it is possible to estimate the capability of the SBCs in reproducing a mean shoreline (see figure 3.3). The shoreline reproduced with the proposed SBCs is really close to the one obtained with $\mathrm{ROMS_{rs}}$. The wave run-up phase is mainly forced

by the Riemann function (R_+) which dominates on both the second ($\sqrt{2gH}$) and the third terms (the swash-zone volume time-derivate) of equation (2.21a) (figure 3.4). Whereas the run-down phase seems to be driven by the third term, when it turns negative, and the first and the second terms cancel each other out. This means that at least for the present test case, even if small, the swash-zone volume time-derivate plays a crucial role to properly represent the shoreline motion. The shoreline run-up (see figure 3.3), is totally in agreement with the stable set-up represented in figure (3.2 top-right panel): after a spin-up of about two minutes, they both become almost constants.

Test case 2

Test case two, was performed with the aim of observing the behavior of $\text{ROMS}_{\text{SBCs}}$ and ROMS_{rs} when forced by a periodic low-frequency signal. The mean shoreline oscillation calculated from both $\text{ROMS}_{\text{SBCs}}$ and ROMS_{rs} are consistent to the incoming wave train having its same period.

The shorelines computed with the two versions of ROMS, have an excursion of about $L_0/3$. At a first glance this may be seen as something weird, since the maximum wave height for this test case was just about $d_0/5$. However, this is probably a function of the low bed friction (quadratic bottom drag coefficient of 0.005) and the really gentle sloping beach (1/80) used for this work.

Using the proposed SBCs, allowed us to reproduce a shoreline close to the one obtained by ROMS_{rs} (reference solution with about $L_0/120$ cross-shore resolution), but using a much coarser grid of about $L_0/3$. At the coarsest resolution of about $L_0/2$ even the proposed SBCs cannot properly represent x_l.

Notwithstanding the shorelines are really similar both in shape and size, there is a clear forward time shift of the shorelines calculated with $\text{ROMS}_{\text{SBCs}}$ with reference to the one obtained with ROMS_{rs}. Looking at the really beginning of the simulations (fig-

ure 3.7) carried with grids coarser than $L_0/5$, one may think that the time shift observed is due to the strong initial perturbation of the shoreline computed with $\mathrm{ROMS_{SBCs}}$, which propagates over the whole simulation length. Further considerations, can lead to infer that the time shift is totally or partially generated by some effect of the different time steps used ($T_0/40$ for the grid made with about 120 and 50 nodes per L_0 and $T_0/4$ for the other grid resolutions) for the simulations. However, our results are not designed to properly answer this question, and further investigation is needed in this direction.

Test case 3

With the last test case, we wanted to more closely investigate the behavior of the shoreline when calculated with the proposed SBCs. Here, we use a wave train with a shape changing as a sine function, in order to conform our work with the ones that are normally found in literature.

As for the other experiments, the shoreline was well reproduced with $\mathrm{ROMS_{SBCs}}$ up to a resolution of about 1.5 nodes per wavelength where, the shoreline started to have an oscillation frequency higher than the one from $\mathrm{ROMS_{rs}}$. The Fourier analysis performed on the shoreline computed with $\mathrm{ROMS_{SBCs}}$ at the resolution of $L_0/2$ (figure 3.27) clearly shows a frequency band broader when compared with the one of our reference solution (figure 3.23). Such higher frequency is somehow the reflection of the perturbations of all the terms of the right-hand side of equation (2.21a) (figure 3.15f and figure 3.28). Seams to be obvious that these instabilities are artificial numerically generated signals. However, the dominant influence on the shoreline behavior seems to be that of the first term. However, it must be noted, that opportunely filtering, would make possible to reconstruct the shoreline oscillation also at the coarsest resolution.

The spatial and time scales of the phenomena evolving in really

shallow waters are small and need to be calculated at high time and spatial resolutions. Thus, terms like the radiation stress, which is a fundamental forcing of the SBCs, may not be properly computed with too coarse resolutions this causing problems also in the assessment of the shoreline motion.

The shoreline oscillation, is mainly due to the differences between the first term and the second term of equation (2.21a), with the third term (the swash zone volume time-derivate) that accelerates the shoreline during the run-up and decelerates it during the run-down (see figure 3.15).

The characteristic curves incoming at x_l are almost straight lines, the characteristics receding from the shoreline are not. The characteristic curves are given by integration of equation (2.23), which represents the characteristic speed. One possible explanation of these different shapes, can be sought by trying to understand which of the two terms, $\bar{u}$ and c dominates in the integration of (2.23). The cross-shore phase speed c at different time levels is shown in figure 4.1. We can see that c, more or less, decreases with the same slope both: during the run-up and during the run-down. The same is not true for $\bar{u}$ which, relatively close to the shoreline, is always positive and gently nonlinearly decreasing during the run-up. Whereas, during the run-down, it is negative and quickly decreases. Thus, the curvature of the receding characteristics is probably caused by the stronger deceleration due to $\bar{u}$ during the run-down.

4.2 Integral model parametrization

The swash zone volume

The sensitivity analysis for the Cv function (figure 3.18), has revealed that the tuning of this parameter within a certain range of values, is not of crucial importance for the estimation of the shoreline. However, it weakly contributes to shape of the shoreline throughs.

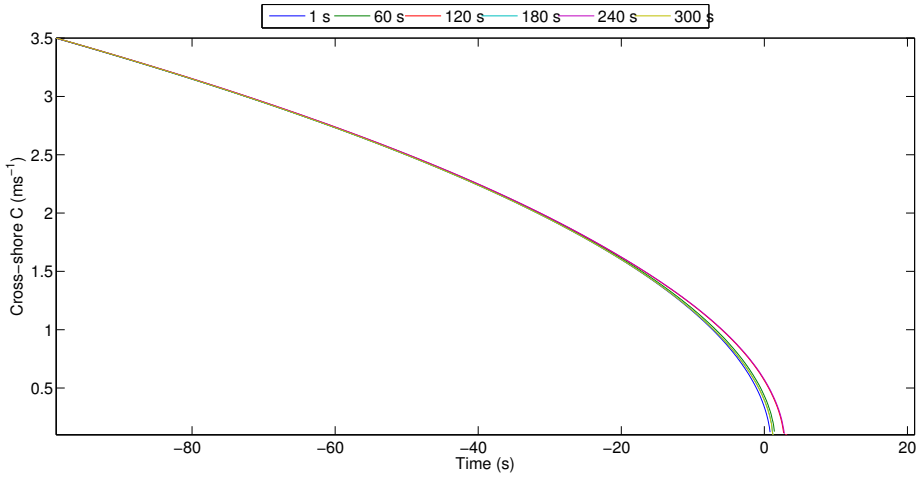

Figure 4.1: Mid domain cross-shore section at different times of the phase speed c (resolution of about $L_0/120$; wave height from equation (3.1)).

The absence of the swash zone volume time derivative (figure 3.19) in equation (2.21a) did not give the result expected. What we would expect, was a wider oscillation of the shoreline due to the absence of the deceleration imposed by the swash zone volume during the run-up and the absence of accelerations from the swash zone volume during the run-down. This, somehow, is not what happens. Conversely the shoreline oscillation obtained with no swash zone volume, is slightly smaller than the one computed with the 'full' version of equation (2.21a). This is probably due to the fact that the swash zone volume does not decelerate the shoreline for the whole duration of the run-up but, at a certain point toward the end of the run-up, it starts to accelerate it. The other way round is true for the run-down.

For the first test case, the swash zone volume seems to have a crucial role for a good assessment of the shoreline by means of the proposed SBCs, however, for the others two numerical experiments, the swash zone volume seems to have a more marginal role. The swash zone volume for all the simulation is in the order of mm^2 (data not shown), these because most of the waves energy have

already dissipate before reaching the shoreline. With a such small swash zone volume, it is not surprising that the shoreline is not strongly affected by it, thus, it almost behaves as a moving rigid wall (sea Brocchini and Peregrine 1996 for a definition of moving rigid wall). It is obvious that further investigations are needed to clarify the importance of the swash zone volume for the computation of shoreline motion.

The Riemann function

When starting the propagation of R_+ too far from the shoreline (figure 3.20a, figure 3.21a, and figure 3.22a), the shoreline shifts seaward because the difference between the first term and the second term of equation (2.21a) becomes smaller. Whereas, starting the propagation of R_+ too close to the shoreline (figure 3.20d, figure 3.21d, and figure 3.22d) leads to a wider shoreline oscillation due to an overestimation of R_+ at x_l. The best result is clearly achieved when the propagation of R_+ starts at a location where at least 5% of the waves started breaking (figure 3.20b, figure 3.21b, and figure 3.22b).

Modifying the code in order to allow for the propagation of R_+ from the location where a given percentage of waves start to break, led to a better computation of the shoreline motion. Our analysis also confirms, in agreement with Brocchini and Bellotti (2002), that an accurate computation of R_+ at the shoreline is the most crucial issue for correctly predicting the motion of the mean shoreline.

4.3 Wrap up section

In the following we briefly summarize the main findings of our work.

Running ROMS at really high resolutions, allows to reach the shoreline, where the artificial shoreline condition of rigid wall describes well the shoreline motion.

Such simulations are really time consuming and computational

effort requiring, thus, are not useful from a practical point of view. However, they allowed us to carry out a benchmark solution to assess the value of the proposes SBCs .

Using the proposed SBCs allowed us to reproduce a shoreline close to the one obtained by $\mathrm{ROMS_{rs}}$, achieved with $L_0/120$ cross-shore resolution, but using a much coarser grid of $L_0/3$. At the coarsest resolution of about $L_0/2$ even the proposed SBCs cannot properly represent x_l.

The importance of the swash zone volume term for the motion of x_l, seems to change across different numerical experiments. Thus, further investigations are needed to clarify its importance. Whereas the importance of the starting point for the inshore propagation of R_+ seems clear. The spatial and time scales of the phenomena evolving in really shallow waters are small and need to be calculated at high time and spatial resolutions. Thus, terms like the radiation stress, which is a fundamental forcing of the SBCs, may not be properly computed with too coarse resolutions, this causing problems also in the assessment of the shoreline motion.

The time needed for the simulation run with $\mathrm{ROMS_{rs}}$ at $L_0/120$ cross-shore resolution is in the order of some hours, while the one carried with $\mathrm{ROMS_{SBCs}}$ at a $L_0/3$ cross-shore resolution in the order of some minutes. Hence, the great advantage, in terms of computational costs, of using the proposed SBCs is very evident. We believe that this work is a really important step toward the inclusion of the swash zone dynamic into nearshore models. The SBCs from the integral theoretical model have been successfully calculated within the kernel of a wave averaging model for the first time. This using flow properties coming from the off-shore of the computational domain. However some further effort need to be addressed to actually force the model with the use of the SBCs. Thus assess the effect of the swash zone dynamic into the nearshore area.

List of symbols

α	Beach slope
$\bar{\eta}$	Mean water elevation
$\bar{u}$	Mean cross-shore flow velocity
$\langle d \rangle$	Long-wave contribution to the water depth
$\langle u \rangle$	Long-wave contribution to the cross-shore velocity
$\langle v \rangle$	Long-wave contribution to the long-shore velocity
η	Water free surface
ω	Angular frequency
σ	Relative radian frequency
θ	Wave direction
$\tilde{d}$	Short-wave contribution to the water depth
$\tilde{u}$	Short-wave contribution to the cross-shore velocity
$\tilde{v}$	Short-wave contribution to the long-shore velocity
a	Wave amplitude
BC_{ts}	Baroclinic time step
BT_{ts}	Barotropic time step
C	Wave celerity

c	Wave celerity in shallow water
C_+	Positive characteristic curves
c_σ	Propagation speed in frequency space
c_θ	Propagation speed in directional space
c_x	Wave group celerity, x-direction
c_y	Wave group celerity, y-direction
d	Water depth
d_{crit}	Spatially-constant user-defined critical minimum for the wetting-drying process depth
E	Wave energy density
g	Gravitational acceleration
H	Wave height
H_0	Offshore wave height
H_{max}	Maximum off-shore wave height
k	Wavenumber
L	Wave wavelength
L_0	Offshore wavelength
N	Action density spectrum
R_+	Positve Riemann function
S_{11}	Vertically integrated, wave-averaged cross-shore radiation stress
S_w	Sources and sinks of wave energy density
T	Wave period

T_0	Off-shore incident wave period
T_s	Swash period
T_{tr}	Wave train period
u	Cross-shore component of the velocity
u_s	Ocean surface currents, x-direction
$ubar$	Mean flow velocity, x-direction
v	Long-shore component of the velocity
v_s	Ocean surface currents, y-direction
$vbar$	Mean flow velocity, y-direction
W	Long-wave contribution to the long-shore flow velocity inside the surf zone
x	Crossshore Horizontal coordinate
x_c	Crosshore horizontal coordinate of generic point along C_+
x_h	Cross-shore coordinate of the shoreward swash zone limits
x_l	Cross-shore coordinate of the seaward swash zone limits
x_s	Crosshore coordinate of the instantaneous shoreline
x_{ROMS}	Position of the last dry node in the computational domain
y	Long-shore Horizontal coordinate

Bibliography

Airy, GB (1841). *Tides and Waves*. J.J. Griffin.

Antuono, M, M Brocchini, and G Grosso (2007). "Integral properties of the swash zone and averaging. Part 3. Longshore shoreline boundary conditions for wave-averaged nearshore circulation models". In: *Journal of Fluid Mechanics* 573, pp. 399–415.

Baldock, TE, P Holmes, and DP Horn (1997). "Low frequency swash motion induced by wave grouping". In: *Coastal Engineering* 32.2, pp. 197–222.

Battjes, JA and JPFM Janssen (1978). "Energy loss and set-up due to breaking of random waves". In: *Coastal Engineering Proceedings* 1.16.

Bellotti, G and M Brocchini (2005). "Swash zone boundary conditions for long-wave models". In: *Coastal engineering* 52.10, pp. 971–976.

Bingham, HB, PA Madsen, and DR Fuhrman (2009). "Velocity potential formulations of highly accurate Boussinesq-type models". In: *Coastal Engineering* 56.4, pp. 467–478.

Booij, N, RC Ris, and Leo H Holthuijsen (1999). "A third-generation wave model for coastal regions: 1. Model description and validation". In: *Journal of Geophysical Research: Oceans* 104.C4, pp. 7649–7666.

Boussinesq, J (1872). "Théorie des ondes et des remous qui se propagent le long d'un canal rectangulaire horizontal, en communiquant au liquide contenu dans ce canal des vitesses sensiblement pareilles de la surface au fond." In: *Journal de Mathématiques Pures et Appliquées*, pp. 55–108.

Brocchini, M (1997). "Eulerian and Lagrangian aspects of the longshore drift in the surf and swash zones". In: *Journal of Geophysical Research: All series* 102, pp. 23–155.

– (2013). "A reasoned overview on Boussinesq-type models: the interplay between physics, mathematics and numerics". In: *Proceedings of the Royal Society of London A: Mathematical, Physi-*

cal and Engineering Sciences. Vol. 469. 2160. The Royal Society, p. 20130496.

Brocchini, M and TE Baldock (2008). "Recent advances in modeling swash zone dynamics: Influence of surf-swash interaction on nearshore hydrodynamics and morphodynamics". In: *Reviews of Geophysics* 46.3.

Brocchini, M and G Bellotti (2002). "Integral flow properties of the swash zone and averaging. Part 2. Shoreline boundary conditions for wave-averaged models". In: *Journal of Fluid Mechanics* 458, pp. 269–281.

Brocchini, M and DH Peregrine (1996). "Integral flow properties of the swash zone and averaging". In: *Journal of Fluid Mechanics* 317, pp. 241–273.

Butt, T and P Russell (1999). "Suspended sediment transport mechanisms in high-energy swash". In: *Marine Geology* 161, pp. 361–375.

– (2000). "Hydrodynamics and cross-shore sediment transport in the swash-zone of natural beaches: a review". In: *Journal of Coastal Research*, pp. 255–268.

Cowell, PJ (1982). *Breaker stages and surf structure on beaches*. Coastal Studies Unit, Department of Geography, the University of Sydney.

De Vriend, HJ and MJF Stive (1987). "Quasi-3D modelling of nearshore currents". In: *Coastal Engineering* 11.5-6, pp. 565–601.

Ebersole, Bruce A and Robert A Dalrymple (1980). "Numerical modelling of nearshore circulation". In: *Coastal Engineering Proceedings* 1.17.

Elfrink, B and TE Baldock (2002). "Hydrodynamics and sediment transport in the swash zone: a review and perspectives". In: *Coastal Engineering* 45.3, pp. 149–167.

Galvin, Cyril J (1968). "Breaker type classification on three laboratory beaches". In: *Journal of Geophysical Research* 73.12, pp. 3651–3659.

Goda, Yoshimi (1975). “Irregular wave deformation in the surf zone”. In: *Coastal Eng. Japan* 18, pp. 13–25.

Guza, RT and EB Thornton (1982). “Swash oscillations on a natural beach”. In: *Journal of Geophysical Research: Oceans* 87.C1, pp. 483–491.

Haas, KA, IA Svendsen, et al. (2003). “Quasi-three-dimensional modeling of rip current systems”. In: *Journal of Geophysical Research: Oceans* 108.C7.

Haas, KA and JC Warner (2009). “Comparing a quasi-3D to a full 3D nearshore circulation model: SHORECIRC and ROMS”. In: *Ocean Modelling* 26, pp. 91–103.

Haidvogel, DB et al. (2008). “Ocean forecasting in terrain-following coordinates: Formulation and skill assessment of the Regional Ocean Modeling System”. In: *Journal of Computational Physics* 227.7, pp. 3595–3624.

Hedström, KS (2016). *Technical manual for a Coupled Sea-Ice/Ocean Circulation Model (Version 4)*. U.S. Dept. of the Interior, Bureau of Ocean Energy Management, Alaska OCS Region: OCS Study BOEM 2016-037, p. 176.

Hibberd, S and DH Peregrine (1979). “Surf and run-up on a beach: a uniform bore”. In: *Journal of Fluid Mechanics* 95.02, pp. 323–345.

Holman, RA (1986). “Extreme value statistics for wave run-up on a natural beach”. In: *Coastal Engineering* 9.6, pp. 527–544.

Holthuijsen, Leo H (2010). *Waves in oceanic and coastal waters*. Cambridge University Press.

Hughes, MG, G Masselink, and RW Brander (1997). “Flow velocity and sediment transport in the swash zone of a steep beach”. In: *Marine Geology* 138.1, pp. 91–103.

Huntley, DA (1976). “Long-period waves on a natural beach”. In: *Journal of Geophysical Research* 81.36, pp. 6441–6449.

Huntley, DA, RT Guza, and AJ Bowen (1977). “A universal form for shoreline run-up spectra?” In: *Journal of Geophysical Research* 82.18, pp. 2577–2581.

Jacob, R, J Larson, and E Ong (2005). "M x N communication and parallel interpolation in CCSM using the Model Coupling Toolkit". In: *Preprint ANL/MCSP1225-0205. Mathematics and Computer Science Division, Argonne National Laboratory* 25.

Kaminsky, GM and NC Kraus (1993). "Evaluation of depth-limited wave breaking criteria". In: *Ocean Wave Measurement and Analysis*. ASCE, pp. 180–193.

Korteweg, DJ and G De Vries (1895). "XLI. On the change of form of long waves advancing in a rectangular canal, and on a new type of long stationary waves". In: *The London, Edinburgh, and Dublin Philosophical Magazine and Journal of Science* 39.240, pp. 422–443.

Larson, J, R Jacob, and E Ong (2005). "The model coupling toolkit: a new Fortran90 toolkit for building multiphysics parallel coupled models". In: *International Journal of High Performance Computing Applications* 19.3, pp. 277–292.

Longuet-Higgins, MS (1970). "Longshore currents generated by obliquely incident sea waves: 2". In: *Journal of Geophysical Research* 75, pp. 6790–6801.

Longuet-Higgins, MS and RW Stewart (1964). "Radiation stresses in water waves; a physical discussion, with applications". In: *Deep Sea Research and Oceanographic Abstracts*. Vol. 11. 4. Elsevier, pp. 529–562.

Madsen, PA, HB Bingham, and HA Schäffer (2003). "Boussinesq-type formulations for fully nonlinear and extremely dispersive water waves: derivation and analysis". In: *Proceedings of the Royal Society of London A: Mathematical, Physical and Engineering Sciences*. Vol. 459. 2033. The Royal Society, pp. 1075–1104.

Madsen, PA, DR Fuhrman, and B Wang (2006). "A Boussinesq-type method for fully nonlinear waves interacting with a rapidly varying bathymetry". In: *Coastal Engineering* 53.5, pp. 487–504.

Mase, H (1995). "Frequency down-shift of swash oscillations compared to incident waves". In: *Journal of Hydraulic Research* 33.3, pp. 397–411.

Masselink, G and JA Puleo (2006). "Swash-zone morphodynamics". In: *Continental Shelf Research* 26.5, pp. 661–680.

Mei, CC (1989). *The applied dynamics of ocean surface waves.* Vol. 1. World scientific.

Mellor, GL (2008). "The depth-dependent current and wave interaction equations: a revision". In: *Journal of Physical Oceanography* 38.11, pp. 2587–2596.

Miles, John W (1957). "On the generation of surface waves by shear flows". In: *Journal of Fluid Mechanics* 3.02, pp. 185–204.

Munk, W (1949). "Surf beats". In: *EOS, Transactions American Geophysical Union* 30.6, pp. 849–854.

Noda, EK (1974). "Wave-induced nearshore circulation". In: *Journal of Geophysical Research* 79, pp. 4097–4106.

Özkan-Haller, HT and JT Kirby (1997). "A Fourier-Chebyshev collocation method for the shallow water equations including shoreline runup". In: *Applied Ocean Research* 19.1, pp. 21–34.

Peregrine, DH (1967). "Long waves on a beach". In: *Journal of Fluid Mechanics* 27.04, pp. 815–827.

– (1972). "Equations for water waves and the approximations behind them". In: *Waves on beaches and resulting sediment transport*, pp. 95–121.

Peregrine, DH and SM Williams (2001). "Swash overtopping a truncated plane beach". In: *Journal of Fluid Mechanics* 440, pp. 391–399.

Phillips, Owen M (1957). "On the generation of waves by turbulent wind". In: *Journal of Fluid Mechanics* 2.5, pp. 417–445.

Puleo, JA et al. (2000). "Swash zone sediment suspension and transport and the importance of bore-generated turbulence". In:

Putrevu, U and IA Svendsen (1999). "Three-dimensional dispersion of momentum in wave-induced nearshore currents". In: *European Journal of Mechanics - B/Fluids* 18, pp. 409–427.

Raubenheimer, B and RT Guza (1996). "Observations and predictions of run-up". In: *Journal of Geophysical Research: Oceans* 101.C11, pp. 25575–25587.

Shannon, Claude Elwood (1949). “Communication in the presence of noise”. In: *Proceedings of the IRE* 37.1, pp. 10–21.

Shchepetkin, AF and JC McWilliams (2005). “The regional oceanic modeling system (ROMS): a split-explicit, free-surface, topography-following-coordinate oceanic model”. In: *Ocean Modelling* 9.4, pp. 347–404.

– (2009). “Correction and commentary for “Ocean forecasting in terrain-following coordinates: Formulation and skill assessment of the regional ocean modeling system” by Haidvogel et al., J. Comp. Phys. 227, pp. 3595–3624”. In: *Journal of Computational Physics* 228.24, pp. 8985–9000.

Shen, MC and RE Meyer (1963). “Climb of a bore on a beach Part 3. Run-up”. In: *Journal of Fluid Mechanics* 16.01, pp. 113–125.

Stokes, GG (1847). “On the theory of oscillatory waves”. In: *Transactions of the Cambridge Philosphical Society* 8, pp. 441–473.

Svendsen, IA (1984). “Mass flux and undertow in a surf zone”. In: *Coastal Engineering* 8, pp. 347–365.

Svendsen, IA, KA Haas, and Q Zhao (2002). “Quasi-3D nearshore circulation model SHORECIRC”. In: *Center for Appl. Coastal Res., Univ. of Delaware, Internal Rep., CACR-02–01, Newark, DE.*

Svendsen, IA and RS Lorenz (1989). “Velocities in combined undertow and longshore currents”. In: *Coastal Engineering* 13, pp. 55–79.

Svendsen, IA, PA Madsen, and JB Hansen (1978). “Wave characteristics in the surf zone”. In: *Coastal Engineering Proceedings* 1.16.

Svendsen, IA and U Putrevu (1990). “Nearshore circulation with 3-D profiles”. In: *Coastal Engineering Proceedings* 1.22.

– (1994). “Nearshore mixing and dispersion”. In: *Proceedings of the Royal Society of London A: Mathematical, Physical and Engineering Sciences.* Vol. 445. 1925. The Royal Society, pp. 561–576.

Symonds, G, DA Huntley, and AJ Bowen (1982). "Two-dimensional surf beat: Long wave generation by a time-varying breakpoint". In: *Journal of Geophysical Research: Oceans* 87.C1, pp. 492–498.

Tucker, MJ (1950). "Surf beats: sea waves of 1 to 5 min. period". In: *Proceedings of the Royal Society of London A: Mathematical, Physical and Engineering Sciences*. Vol. 202. 1071. The Royal Society, pp. 565–573.

Uchiyama, Y, JC McWilliams, and AF Shchepetkin (2010). "Wave–current interaction in an oceanic circulation model with a vortex-force formalism: Application to the surf zone". In: *Ocean Modelling* 34.1, pp. 16–35.

Ursell, F (1953). "The long-wave paradox in the theory of gravity waves". In: *Mathematical Proceedings of the Cambridge Philosophical Society*. Vol. 49. 04. Cambridge Univ Press, pp. 685–694.

Veeramony, J and IA Svendsen (2000). "The flow in surf-zone waves". In: *Coastal Engineering* 39, pp. 93–122.

Warner, JC et al. (2013). "A wetting and drying scheme for ROMS". In: *Computers & Geosciences* 58, pp. 54–61.

Whitham, GB (1958). "On the propagation of shock waves through regions of non-uniform area or flow". In: *Journal of Fluid Mechanics* 4.04, pp. 337–360.

Wright, LD, RT Guza, and AD Short (1982). "Dynamics of a high-energy dissipative surf zone". In: *Marine geology* 45.1-2, pp. 41–62.

Wright, LD and AD Short (1984). "Morphodynamic variability of surf zones and beaches: a synthesis". In: *Marine geology* 56.1-4, pp. 93–118.

Wu, CS and PL Liu (1985). "Finite Element Modeling of Nonlinear Coastal Currents". In: *Journal of Waterway Port Coastal and Ocean Engineering* 111, pp. 417–432.